

Wind Turbine Control Co-Design Using Dynamic System Derivative Function Surrogate Model (DFSM) Based on OpenFAST Linearization*

Yong Hoon Lee^{a,1,*}, Saeid Bayat^{b,1}, James T. Allison^c

^a*Mechanical Engineering, The University of Memphis, Memphis, TN 38152, USA*

^b*Naval Architecture & Marine Engineering, University of Michigan, Ann Arbor, MI 48109, USA*

^c*Industrial and Enterprise Systems Engineering, University of Illinois at Urbana-Champaign, Urbana, IL 61801, USA*

Abstract

This research presents a comprehensive control co-design (CCD) framework for wind turbine systems, integrating nonlinear derivative function surrogate models (DFSMs) developed through OpenFAST linearization and data-driven approaches. The primary motivation for developing the DFSM is to accurately capture the nonlinear dynamics of wind turbine systems in a computationally efficient manner, thereby enabling effective and scalable optimization within the CCD framework. The developed DFSMs successfully represent state derivatives and system output responses across extensive plant, control, and state variables ranges, validated against direct simulation outputs. By concurrently optimizing plant and control designs, the CCD approach leverages their synergistic interactions, resulting in significant reductions in the levelized cost of energy (LCOE) through an optimized balance of annual energy production (AEP) and costs associated with plant design parameters, while adhering to design and physical constraints. Comparative analyses demonstrate that CCD, particularly when utilizing open-loop optimal control (OLOC), outperforms traditional closed-loop control (CLC) strategies. Sensitivity and sparsity analyses reveal critical interdependencies among design variables, emphasizing key input-output parameter relationships that guide targeted design optimizations. These studies build on pioneering DFSM work that was limited to a handful of design and state variables; this work advances DFSM capabilities to the level of practical utility in engineering design for the first time. This work presented here serves as a foundational exploration; authors advocate for future research to incorporate broader constraints and other considerations to further advance CCD methodologies for wind turbine system optimization.

Keywords:

derivative function surrogate modeling (DFSM), control co-design (CCD), open-loop optimal control (OLOC), wind turbine, design optimization

1. Introduction

Developing highly efficient large-scale wind turbine systems requires a system description that accurately captures the real-world behavior of the coupled system. Furthermore, it requires design methodolo-

*A part of this work contains the research outcome presented at the Applied Energy Symposium: MIT A+B 2022, Cambridge, MA, USA (online).

*Corresponding author. Email: yhlee@memphis.edu, Address: 312 Engineering Science Bldg, Memphis, TN 38152-3180

¹These two authors contributed equally to this work.

gies that thoroughly explore the complex design space while accounting for the system’s inherent design coupling. Many researchers in renewable energy have recently investigated the technical possibilities and innovative potential of an integrated plant (physical domain) and control design methodology [1–7], often referred to as control co-design (CCD) [5, 7–10]. The CCD approach redefines the principles of wind turbine design by leveraging synergistic interfacial couplings between the physical and control domains, thereby exceeding the possibilities offered by traditional sequential design approaches, where the physical system is designed and then the control is tuned for the already designed plant. Although the significance of applying CCD to wind energy systems is well established in recent literature, its practical implementation has encountered certain limitations [1, 10]. This paper aims to address several of these limitations, including modeling approaches, control schemes, objective function formulations, plant design variables, and constraints, among other aspects.

In this context, Sect. 1.1 provides a thorough review of existing literature, identifying critical limitations in prior CCD methodologies for wind turbine systems. In Sect. 1.2, we outline the considerations and approaches adopted in this study to overcome these challenges. Section 2 introduces the methods and models used to construct the proposed framework, while Sect. 3 presents the problem formulation and optimization procedures. The results of various optimization scenarios are analyzed in Sect. 4. Finally, in Sect. 5, we conclude with key findings and discuss their implications for practical applications and future research needs.

1.1. Literature Review

Numerous early and ongoing research efforts interpret the term CCD in varying ways, often adopting practical yet limited approaches to the concept. For instance, some studies focus exclusively on control design, often neglecting the critical interactions with plant design [11]. Others employ sequential or iterative sequential design methods that, while providing valuable practical design insights, do not necessarily guarantee convergence to a system-optimal CCD solution [1]. Simplified modeling approaches, such as frequency domain analysis, can be advantageous for broader design exploration during early-stage design processes [12, 13]. However, these methods may struggle to capture critical system dynamic behaviors, which are particularly important in floating offshore wind turbine (FOWT) CCD solutions. Additionally, some studies restrict their CCD applications to limited design load cases (DLCs), such as focusing on a single wind speed profile [14, 15]. While this simplification can facilitate analysis and provide initial insights, it fails to capture the realistic variability of objective and constraint function values encountered in practical scenarios.

Regarding wind turbine control design, previous studies have focused primarily on designing and tuning relatively simple closed-loop controllers (CLCs) [1, 11, 13, 16–19]. Meanwhile, some articles have explored advanced controllers and optimal control approaches, such as model predictive control (MPC) [20, 21] and open-loop optimal control (OLOC) [4, 5, 14, 15]. OLOC computes an entire control trajectory in advance by optimizing it over a finite (fixed or variable) time horizon without using real-time feedback during execution. Furthermore, regardless of the control scheme employed, many studies have focused on optimizing only one control signal, often the generator torque or blade pitch, rather than a more holistic control perspective [13–16, 22].

Modern utility-scale turbines mostly employ CLCs as their primary control loop, including simple proportional-integral (PI) or proportional-integral-derivative (PID) controllers, due to their simplicity and practical effectiveness. CLCs provide tunability and feedback control capability in controlling generator, yaw motor, and blade pitch actuators [23]. These easy-to-implement characteristics and cost-effectiveness make CLCs widespread in industrial controls applications [24–26]. However, their inherent lack of flexibility can constrain efforts to explore system-optimal designs and limit understanding of design trade-offs

during the early stage development. In contrast, while OLOCs are not directly practical because they depend on knowledge of the entire time horizon and do not provide real-time control solutions, they offer greater design flexibility. This flexibility facilitates the discovery of innovative design solutions and insights into the maximum potential of the system [5, 27], which can subsequently inform and refine CLC designs at later development stages [28].

The choice of optimization metrics in previous CCD research is another topic that has been studied from diverse perspectives. Although the levelized cost of energy (LCOE) is a direct and comprehensive metric, many studies have opted for alternative objective functions [29]. In the context of CCD, relatively few studies have optimized LCOE or similar metrics, and even then with limitations [4, 5, 18], largely due to the associated technical complexities and recognized incompleteness of the LCOE metric [30]. Common alternatives include mass [31], annual energy production (AEP) [15, 19, 32], blade root bending moment [11, 33], power quality [13], and weighted combinations of these factors [11, 13, 14, 34]. Motivations for these alternative metrics include mitigating the noise and poor scaling often found in LCOE calculation, which complicate gradient-based optimization, and simplifying scope by concentrating on a single, well-defined objective function [15, 30, 31]. Such alternatives typically emphasize aspects of energy production, system integrity, or cost, while avoiding the additional complexities of computing LCOE.

Prior literature also tends to optimize individual components of wind turbine systems, such as platforms [4], towers [32, 35, 36], blades [1, 18, 33], or farm layouts [19, 37], rather than employing a holistic system model encompassing all key elements. Furthermore, CCD problems in existing research often adopt a limited set of simplified constraints, such as lower and upper bounds of design variables [4, 34]. This focused approach arises from the complex, multidisciplinary integration challenges inherent to wind turbine systems. Accounting for these interactions significantly increases optimization complexity, demanding advanced simulation tools to capture the behaviors of multiple interacting components efficiently, while increasing the risk of convergence to suboptimal designs.

1.2. Strategies Utilized in This Study

Models with first-principles, low-order governing equations [3, 5, 38] or those simplified from higher-fidelity representations, such as linearizations [39, 40], are frequently employed in CCD problems because models that capture the full-scale dynamic response are often computationally too expensive for use in the CCD optimization loop. In particular, for wind turbine design research, many studies have utilized linearized dynamic models encompassing both plant and control domains [4, 14, 39–44]. While these linearized models offer valuable insights, certain limitations must be addressed to ensure accurate and reliable CCD solutions, thereby minimizing the risk of misinterpretation or error beyond acceptable ranges in design processes. Notably, the linear model should be constructed around the center point of the operating range, with states and design variable values kept close to this point to maintain the validity of the linearized approximation [43]. However, this requirement restricts the model’s ability to capture the overall nonlinear behavior of the system, as a single operating point may not represent broader system dynamics. Moreover, large variations in states or exogenous inputs, such as wind speed, often exceed the small deviation range required for model linearity, thereby reducing both the evaluation capability and the design flexibility beyond baseline design.

Another approach to modeling for CCD optimization involves treating the full nonlinear system as a black-box and tuning several key plant and control gain parameters [1, 41, 45]. Numerous wind turbine aero-elasto-hydro-servo simulation tools, including OpenFAST [46], OWENS [47], and Bladed [48], predict nonlinear system behaviors by solving relevant disciplinary domain models in a coupled manner through forward time-domain integration. During this process, instantaneous physical quantities from all disciplines

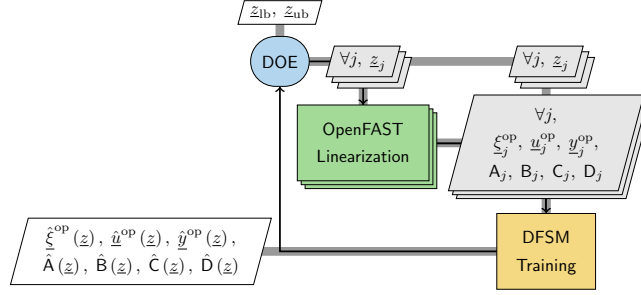


Figure 1: Training procedure of the derivative function surrogate model (DFSM), represented as an extended design structure matrix (XDSM).

are internally coupled via differential-algebraic equations (DAEs), and direct access to local time-derivative variables is typically unavailable (which is needed for important classes of CCD solution strategies [9]).

Given this simulation structure and the “fully packaged” nature of these modeling tools, optimization problems are generally formulated and solved independently of the simulation loop [45]. Additionally, when a specific controller, such as a PID controller, is incorporated, it is often infeasible to perturb the control trajectory to determine the sensitivity of the overall system response. As a result, exploring both plant and control designs within the time integration process, e.g., via direct transcription methods [49], becomes impractical. Consequently, CCD problems that rely on black-box simulation tools often use single-shooting formulations, which can be inefficient and may fail to guarantee convergence to optimal solutions, especially in the presence of unstable or highly nonlinear system behaviors [50–53].

Derivative function surrogate modeling (DFSM), first proposed by Deshmukh and Allison [14], combines the strengths of the preceding approaches by leveraging time-derivative information from full, nonlinear, black-box simulations. DFSM has since been applied to a wide range of dynamic systems representation and optimization studies [40, 54–57]. Rather than replacing the entire black-box simulation end response with a surrogate model, DFSM substitutes state- and control-dependent system dynamic governing equation with a surrogate model. Nonetheless, surrogate models typically face scalability challenges, as computational cost can grow exponentially with higher-dimensional inputs. Although DFSM effectively provides derivative function information for computationally expensive nonlinear simulation models, previous implementations have been significantly constrained in several aspects. These include a limited problem scale because the input space for plant and control design parameters is combined into a single system-level derivative function [14, 57]. Furthermore, the control portion of the model still remains linear, limiting its ability to fully capture nonlinear control dynamics [14].

These challenges highlight the need for a nonlinear DFSM capable of accurately representing wind turbine system behaviors while providing the necessary derivative function information. This work addresses these needs by introducing a CCD optimization based on a nonlinear wind turbine system model that employs surrogate models of derivative functions. These surrogate models are constructed from a broad dataset of linearized OpenFAST models spanning a wide range of environmental conditions and design parameter spaces [40].

2. Methods

2.1. Plant Design Variables and DFSM Construction

The DFSM was trained using the OpenFAST model of the IEA 15 MW reference wind turbine [58]; the structure of this model is illustrated in Fig. 1 using an extended design structure matrix (XDSM) [59].

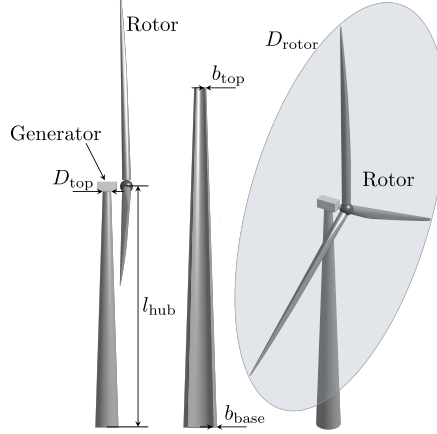


Figure 2: Plant design parameters

Variables (parallelograms) above and next to each disciplinary model (rectangles) represent inputs and outputs of the model, respectively. Training samples were generated within the parameter vector space defined by the lower and upper bounds, \underline{z}_{lb} and \underline{z}_{ub} . The parameter vector (\underline{z}), which serves as the DFSM input, consists of five plant design parameters and one exogenous input variable. The plant parameter vector (\underline{z}_p) includes five key plant design variables: hub height (l_{hub}), tower top diameter (D_{top}), tower bottom thickness (b_{base}), tower top thickness (b_{top}), and rotor diameter (D_{rotor}), while the exogenous input parameter is the wind speed at the hub location (v). Thus, the parameter vector for the DFSM is given as:

$$\begin{aligned} \underline{z} &= \left[\underline{z}_p^T, v \right]^T \\ &= \left[l_{hub}, D_{top}, b_{base}, b_{top}, D_{rotor}, v \right]^T, \end{aligned} \quad (1)$$

and these variables are also illustrated in Fig. 2. For this study, the lower and upper bounds of these parameters were defined around the reference turbine design, given as:

$$\begin{aligned} \underline{z}_{lb} &= [150.0, 4.0, 0.025, 0.005, 230.0, 3.0]^T, \\ \underline{z}_{ub} &= [155.0, 7.1, 0.045, 0.025, 240.0, 25.0]^T. \end{aligned} \quad (2)$$

Using the enhanced stochastic evolutionary (ESE) space-filling method [60], a total of 500 unique plant design sample points were generated in the five-dimensional hyperspace, $\underline{z}_p \in \mathbb{R}^5$. These points were uniformly distributed within the hyperspace and constrained within the prescribed bounds. For each plant design sample point, 23 periodic steady-state OpenFAST simulation cases were created, spanning from cut-in to cut-out wind speeds, and solved to obtain linear models by leveraging distributed-memory parallel computing.

Due to constraint violations, only 421 of the 500 distinct plant design samples could be successfully evaluated; with 23 wind-speed operating points per design, this yielded 9,683 ($= 421 \times 23$) linear models from the OpenFAST periodic steady-state simulations, which constitute the training dataset. In addition, to assess DFSM performance, a separate test set of 80 distinct plant designs, each evaluated with 23 wind-speed operating points per design, are generated for a total of $80 \times 23 = 1,840$ cases.

2.2. DFSM-based Wind Turbine Dynamic Model

OpenFAST generates a linear time-invariant (LTI) model of the periodic steady-state dynamic responses at a specified operating point, expressed as:

$$\begin{aligned}\dot{\underline{\xi}}(t) &= \mathbf{A} \left[\underline{\xi}(t) - \underline{\xi}^{\text{op}} \right] + \mathbf{B} \left[\underline{u}(t) - \underline{u}^{\text{op}} \right] \\ \underline{y}(t) &= \mathbf{C} \left[\underline{\xi}(t) - \underline{\xi}^{\text{op}} \right] + \mathbf{D} \left[\underline{u}(t) - \underline{u}^{\text{op}} \right] + \underline{y}^{\text{op}}\end{aligned}\quad (3)$$

where $\underline{\xi}$ is the vector of state variables and \underline{y} is the vector of system output variables. The states, controls, and system responses at the operating point ($\underline{\xi}^{\text{op}}$, $\underline{u}^{\text{op}}$, and $\underline{y}^{\text{op}}$) are determined after the simulation converges to a periodic steady-state [39]. Because \mathbf{A} , \mathbf{B} , \mathbf{C} , and \mathbf{D} are time-invariant (constant) matrices, the dynamic model remains valid only for small deviations around the operating point under a fixed plant design and wind speed.

To extend this model, we replace the state- and control-dependent system matrices in the linear model with nonlinear, parameter-varying surrogate matrices, which include additional input parameters for different plant designs and operating conditions. The trained DFSM retains a model structure similar to OpenFAST LTI models but makes the matrices and operating point vectors functions of plant design and instantaneous wind speed. The DFSM-based dynamic model is given by:

$$\begin{aligned}\dot{\underline{\xi}}(t) &= \hat{\mathbf{A}}(\underline{z}) \left[\underline{\xi}(t) - \hat{\underline{\xi}}^{\text{op}}(\underline{z}) \right] + \hat{\mathbf{B}}(\underline{z}) \left[\underline{u}(t) - \hat{\underline{u}}^{\text{op}}(\underline{z}) \right] \\ \underline{y}(t) &= \hat{\mathbf{C}}(\underline{z}) \left[\underline{\xi}(t) - \hat{\underline{\xi}}^{\text{op}}(\underline{z}) \right] + \hat{\mathbf{D}}(\underline{z}) \left[\underline{u}(t) - \hat{\underline{u}}^{\text{op}}(\underline{z}) \right] + \hat{\underline{y}}^{\text{op}}\end{aligned}\quad (4)$$

where a circumflex over a function (of any dimension) indicates an approximation (surrogate model) of that function (e.g., $\hat{\mathbf{A}}(\underline{z})$ is an approximation of the true matrix-valued function $\mathbf{A}(\underline{z})$). The resulting state-space system features two DFSM-derived, parameter-varying matrices that separately capture state-dependent and control-dependent system behaviors.

The linear models were obtained from periodic steady-state OpenFAST simulations in which the National Renewable Energy Laboratory (NREL)'s Reference Open-Source Controller (ROSCO)-generated the controlled dynamic behavior of the wind turbine. Consequently, each linearization captures the closed-loop dynamics of the plant operating under ROSCO's control scheme. Training the DFSM on this collection of linear models therefore yields a surrogate that emulates the combined plant and ROSCO behavior.

The OpenFAST linearization process requires approximately 5 to 30 minutes per case using a 2.5GHz AMD EPYC 7502 processor core, depending on how quickly the dynamics converge to periodic steady-state conditions. Leveraging parallelization, up to 60 linearization cases were solved simultaneously. Completing the 9,683 linearization problems required to build the DFSM training dataset required approximately 50 hours. The outputs of OpenFAST linearization include the vector of nominal values of states ($\underline{\xi}^{\text{op}}$), such as tower fore-aft deflection, tower fore-aft rate, and rotor rotational speed; the vector of nominal control parameter value ($\underline{u}^{\text{op}}$), including generator torque and blade collective pitch angle; vector of nominal OpenFAST output quantities ($\underline{y}^{\text{op}}$), such as thrust force, aerodynamic torque, and moments; and the linearization matrices \mathbf{A} , \mathbf{B} , \mathbf{C} , and \mathbf{D} .

Figure 3 illustrates the performance of the trained DFSM. In Fig. 3(a), the horizontal axis represents the quantity calculated by the OpenFAST simulation, while the vertical axis represents those predicted by the DFSM. The thick gray lines in the background indicate perfect agreement; data points lying on these lines confirm the DFSM's accuracy. The training data appears as small black dots, whereas the test data is shown as hollow squares in distinct colors corresponding to different quantities, including rotor rotational

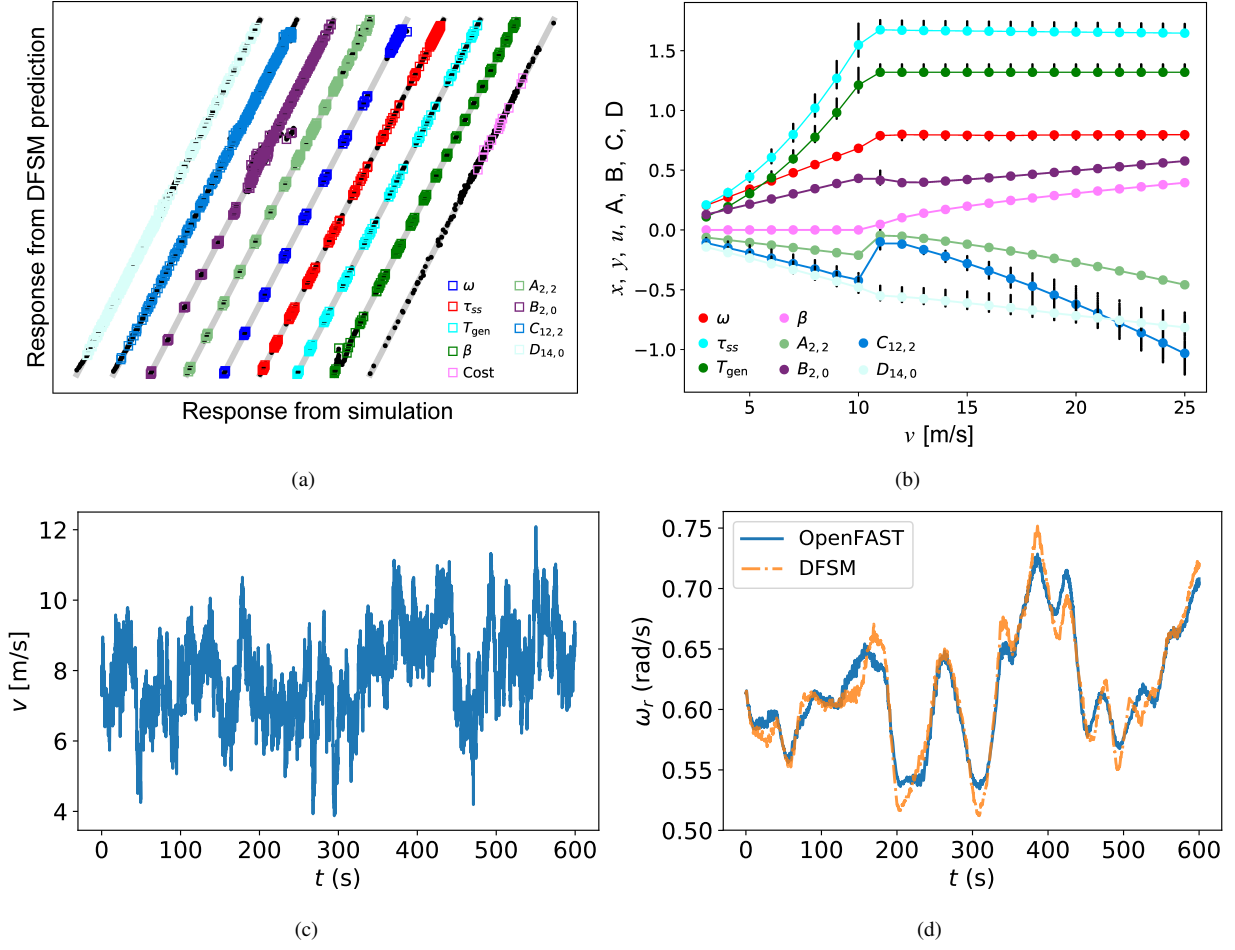


Figure 3: Responses of trained derivative function surrogate models (DFSMs). (a) Predicted responses of DFSMs compared to true simulation responses. (b) Responses of trained DFSMs across varied wind speeds and plant designs. (c) Turbulent inflow wind profile employed for the time-domain comparison between the DFSM and OpenFAST. (d) Comparison of rotor rotational speed time-domain responses predicted by the DFSM and obtained from OpenFAST.

speed (ω), side-to-side moment (τ_{ss}), generator torque (T_{gen}), blade collective pitch angle (β), Cost, and select elements i and j of the matrices A, B, C, and D. These matrix entries are the coefficients that multiply the state and control input variables to produce the corresponding state derivatives and system outputs, representing state-space model. For example, in the rotor-speed derivative formula ($\dot{\omega}_r = A_{2,2}\omega_r + B_{2,0}v + \dots$), coefficient $A_{2,2}$ scales the rotor speed ω_r term, $B_{2,0}$ scales the wind speed v term, and continues. Likewise, coefficient $C_{12,2}$ maps ω_r to the value of tower-base torsional moment $M_{base,tors}$ and $D_{14,0}$ maps wind speed v to the value of tower top side-to-side shear force $F_{top,s-s}$. Although many entries populate these matrices in representing full system dynamics, we plot only representative coefficients that are directly tied to the key performance metrics in Fig. 3. Notably, the predicted quantities closely match the simulation-generated data, demonstrating the effectiveness of the DFSM approach. For the test data points, the mean absolute error and standard deviation are 0.001 and 0.008, respectively.

In Fig. 3(b), selected quantities are shown across wind speeds ranging from cut-in (3 m/s) to cut-out (25 m/s) speeds. The training data appears as small, vertically distributed black dots at each integer wind speed, reflecting plant design variability introduced by 421 distinct plant designs. Notably, some quantities,

such as τ_{ss} , exhibit a stronger correlation with changes in plant design parameters, while others, such as β , remain relatively insensitive to these variations. Large, color-coded circles show the true simulated response of each quantity for a selected plant design at each wind speed level. Solid lines of the matching color illustrate DFSM predictions for the same plant design across the full wind speed range, in 0.01 m/s increments, underscoring the DFSM’s predictive accuracy. Note that the quantities in this figure have been normalized to enhance visualization clarity.

To evaluate how well the trained DFSM reproduces time-domain behavior, we compared its response with that of OpenFAST for a turbulent inflow wind profile with an average of 8 m/s, as shown in Fig. 3(c). The OpenFAST simulation was run for 720 s in total, including a 120 s transient followed by a 600 s analysis window. After discarding the first 120 s, we extracted the control signals from the remaining 600 s data and supplied them to the trained DFSM. Figure 3(d) shows the resulting rotor rotational speed ω_r , demonstrating that the DFSM response closely matches the OpenFAST result, while cutting computational time from roughly 8 minutes to 20 seconds. This substantial speed-up makes the DFSM particularly attractive for CCD studies that require many iterations. Based on the DFSM strategy and responses validated in this section, it is evident that the DFSM demonstrates high accuracy in predicting state derivatives across the combined design and state space; this accuracy is a requirement for utility in finding approximately system-optimal designs when using the DFSM for CCD optimization tasks.

2.3. Insights Obtained From the Trained DFSM

The primary purpose of training the DFSM is to embed it in the CCD framework. However, beyond the primary use, this surrogate model can also reveal insights into how inputs and outputs, including design variables, states, and controls influence to each other, by closely observing sensitivities of output variables, such as cost, power, cost-to-power ratio, tower-top stress (σ_{top}), and tower-base stress (σ_{base}), with respect to the DFSM input vector (\underline{z}), which includes wind speed and five plant design variables. Sensitivities are computed as:

$$S_j = \left\| \frac{y_j(\underline{z}^{i+}) - y_j(\underline{z}^{i-})}{y_j(\underline{z})} \right\|, \quad (5)$$

where, subscript j represents indexes of each output and i denotes indexes of each input. Starting from the output of baseline design at a 10 m/s wind speed, denoted as $y_j(\underline{z})$, each input is perturbed by $\pm 2.5\%$, yielding \underline{z}^{i+} and \underline{z}^{i-} . The resulting 5% spread allows to show which inputs most strongly affect each outputs in terms of sensitivity. The sensitivity S_j is calculated based on this perturbation and normalized by the baseline output.

Figure 4 illustrates the normalized sensitivities S_j of input variables (color-coded in the legend) for each of the five output variables arranged along the horizontal axis. For clearer comparison, the sensitivity bars within each output group are rescaled by that group’s maximum S_j value and the corresponding raw maximum value is printed above the bars. Hence, the most influential input in each group appears at 1.0, and all others are scaled relative to that reference.

As seen in the first group, rotor diameter D_{rotor} is the most sensitive factor that drives cost. Of the two variables defining the tower-top geometry, diameter D_{top} affects cost approximately five times more than wall thickness b_{top} . However, for tower-top stress (fourth group on the horizontal axis), the ratio is roughly 2:1. Hence, thickening b_{top} is generally a cheaper way to satisfy the tower-top stress limit than enlarging D_{top} , which is a trade-off confirmed later in the CCD results.

Power is dominated by wind speed, hub height l_{hub} , and rotor diameter D_{rotor} , in line with established engineering expectations. Higher wind speeds supply more extractable aerodynamic power, a taller hub height exposes the rotor to stronger flows due to atmospheric shear, and a larger rotor diameter expands

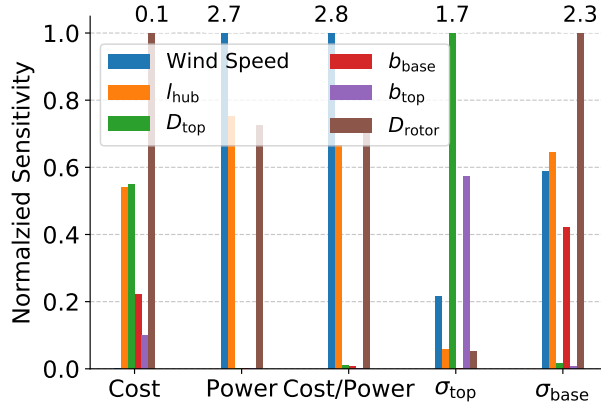


Figure 4: Normalized finite-difference sensitivities S_j of five performance outputs: cost, power, cost to power ratio, tower-top stress, and tower-base stress, to each component of the DFSM input vector: wind speed, hub height, tower-top diameter, tower-base thickness, tower-top thickness, and rotor diameter.

the swept area. These three inputs likewise govern the cost-to-power ratio, whereas the other design variables mainly affect the stress outputs. The plot therefore indicates which variables matter most for each performance metric, the trend confirmed by the CCD results discussed later in Sect. 4.

Another interesting study is to examine the effect of states, wind, and control signals on the state derivatives and outputs. To accomplish this, an in-depth assessment on the influence of time-dependent input variables (e.g., states, controls, and wind speed) on time-dependent output variables (e.g., state derivatives, stresses, and system responses) is presented in Fig. 5. This figure visually conveys the relative importance of each input variable values on the responses or outputs, with darker elements within the matrix indicating stronger connection between the corresponding columns and rows.

Figure 5(a) highlights impact of the state, wind, and control inputs on selected state derivatives (rates of change). Here, x represents the tower fore-aft position, and \dot{x} denotes the tower fore-aft velocity. As previously discussed in Eq. (4), the state derivatives rely on the states, control inputs, and wind speed through the DFSM matrices \hat{A} and \hat{B} . It is evident that the first row (derivative of x , i.e., \dot{x}) is predominantly dependent on the second column (i.e., \dot{x}), which is expected because they convey essentially the same information. Additionally, when examining $\dot{\omega}$, it becomes apparent that it is primarily influenced by wind speed v , followed by blade pitch β , rotor rotational velocity ω , and generator torque T_{gen} .

The system output \underline{y} , comprising 19 distinct time-dependent variables, is interconnected with the systems' states, wind conditions, and control inputs through the DFSM matrices \hat{C} and \hat{D} , as shown in Eq. (4). Figure 5(b) provides insight into the impact of the state, wind, and control inputs on selected system output variables. Here, F_{rotor} is aerodynamic force and T_{rotor} is aerodynamic torque on the wind turbine rotor. Other output variables represent force (F) and moment (M) components at the tower top and base sections, denoted by subscripts "top" and "base," respectively; subsequent subscripts represent fore-aft (f-a), side-to-side (s-s), axial (ax), and torsional (tors) components. It becomes evident that the blade pitch angle (β) exerts the most substantial influence on many of the system outputs. Generator torque T_{gen} significantly affects side-to-side moments at both the tower top and base, as well as aerodynamic torque. Consequently, adjusting generator torque emerges as a key parameter in the optimization problem when aiming to modify these specific forces and moments, aligning with human engineering intuition of the overall wind turbine system. This analysis aids in understanding which input variables play the most pivotal roles in altering the system's output responses.

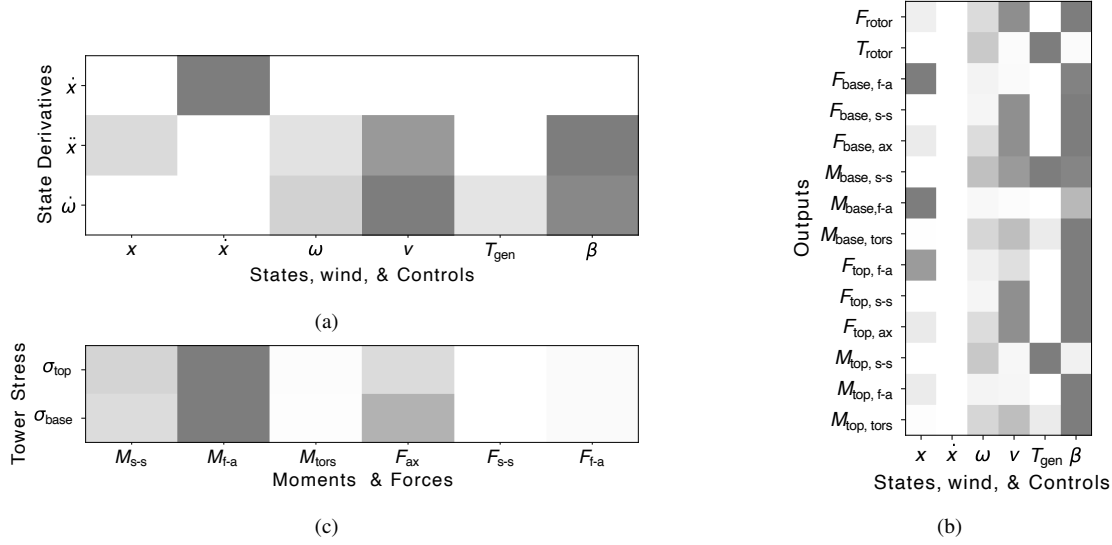


Figure 5: Influence of input variables (horizontal axis, influencing variables) on output variables (vertical axis, influenced variables). Darker cells denote strong influence, while lighter cells represent weaker or negligible influence. (a) Effect of states, wind speed, and control inputs on state derivatives. (b) Effect of the same inputs on various wind turbine system responses (forces and moments). (c) Effect of those forces and moments on tower stresses.

Figure 5(c) illustrates the impact of various moments and forces on the stress experienced by the tower at its top and base sections. Notably, the fore-aft moment M_{f-a} exerts the greatest stress on both the upper and lower sections, while the torsional moment, side-to-side force, and fore-aft force have comparatively minimal effects. As depicted in Fig. 5(b) the primary influencers of M_{f-a} are blade pitch β and fore-aft motion x . Therefore, to manipulate stress within the desired constraints, the optimization problem must adjust these two variables. It is important to note that in this analysis, we exclusively consider von Mises stress; consequently, there could be other criteria where the significance of these other forces may be more influential.

2.4. Operating Environmental Conditions

The Weibull probability density function (PDF) used here to model wind speed distribution is given by:

$$f(v) = \left(\frac{k}{c}\right) \left(\frac{v}{c}\right)^{k-1} \exp\left[-\left(\frac{v}{c}\right)^k\right] \quad (v > 0; k, c > 0), \quad (6)$$

where k is a dimensionless shape parameter and c is the scale parameter in units of wind speed. Because wind speed increases with height, a reference scale parameter c_0 at height H_0 can be used to determine c at any other height H via the power law [61], given by:

$$c = c_0 \left(\frac{H}{H_0}\right)^\alpha. \quad (7)$$

In this study, $k = 2.0$, $\alpha = 0.11$, $c_0 = 11.28$, and $H_0 = 150$ m. Figure 6(a) shows the PDF at two heights (150 m and 155 m). The left vertical axis displays the PDF for both heights, while the right vertical axis indicates the difference between them. As observed, at wind speeds greater than c_0 , the PDF at 155 m exceeds the PDF at 150 m, which affects energy production. This effect is illustrated in Fig. 6(b), where

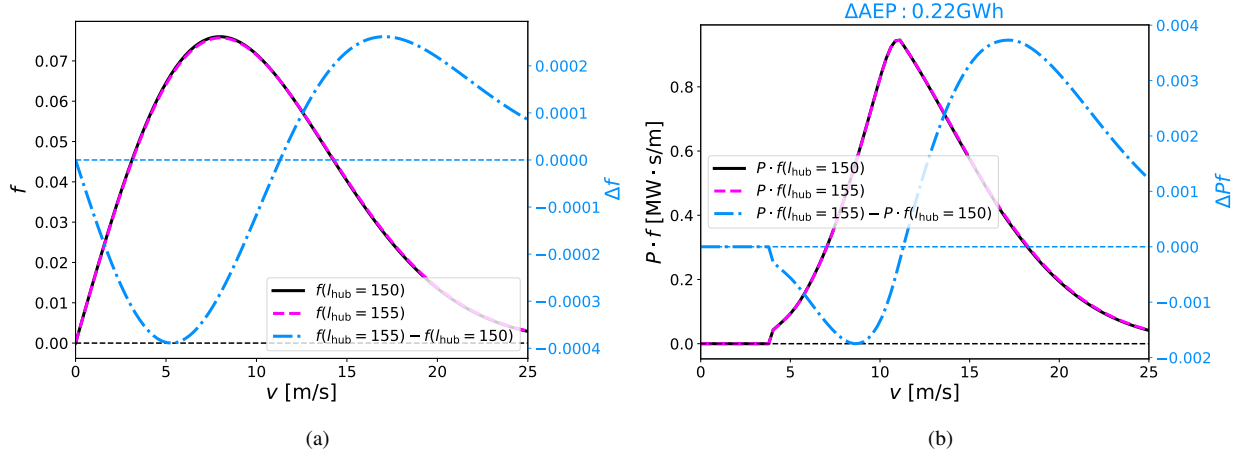


Figure 6: Effect of increasing the baseline wind turbine’s hub height on the Weibull PDF, Pf , and AEP. (a) Comparison of the Weibull PDF and wind speed for the baseline tower when the hub height increases from 150 m to 155 m. (b) Corresponding Pf and resulting changes in AEP.

Pf (the product of power and the Weibull PDF) is plotted for a baseline tower with its height from 150 to 155 m. The slightly higher Pf at 155 m at high wind speeds yields an additional 0.22 GWh of AEP when compared to 150 m.

Using the Weibull distribution, the AEP (in Wh/year) is computed by:

$$AEP = 8760 \int_{v_i}^{v_o} P(v) f(v) dv, \quad (8)$$

where v_o is the cut-out speed, v_i is the cut-in speed, P is the turbine’s output power, and 8,760 is the total number of hours in a year (the product of 365 days and 24 hours/day). In this study, 11 wind profiles representing DLC 1.1 with the normal turbulence model (NTM), as specified in the IEC standard [62], are used. Each profile has different average wind speeds. These profiles appear in Fig. 7(a) as solid lines, with dashed lines indicating their respective mean values. For each wind profile, the PDF is derived according to its mean wind speed, and the turbine’s power output is obtained by simulating a 600-second interval and taking the average power.

Figure 7(b) presents AEP, Cost, and LCOE for six different hub heights, keeping all other parameters at their baseline values. The DFSM is used to predict power generation. The horizontal axis corresponds to hub height, while the vertical axis shows normalized AEP, Cost, and LCOE values relative to the baseline case ($H = 150$ m). As indicated, increasing the hub height boosts both AEP and Cost, but decreases LCOE. Consequently, if there are no explicit constraints that limit the hub height, the optimization naturally converges to higher hub heights.

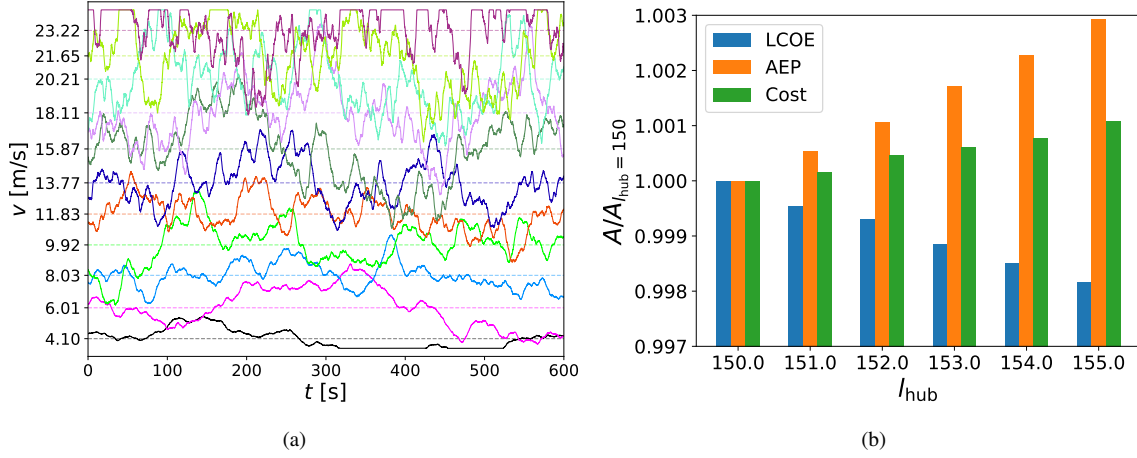


Figure 7: Wind speed profiles used for DLC 1.1, along with the effects of hub height on performance. (a) Eleven wind profiles used for DLC 1.1, each with a distinct average wind speed. (b) Variations in LCOE, AEP, and Cost in response to changes in hub height.

3. Problem Formulation

The problem formulation is presented in Eq. (9), given as:

$$\underset{\underline{z}_p, \underline{u}(t), \underline{\xi}(t)}{\text{minimize}} \quad \text{LCOE}(\underline{z}_p, \underline{u}(t), \underline{\xi}(t)) = \frac{\text{Cost}(\underline{z}_p)}{\text{AEP}(t, \underline{z}_p, \underline{u}(t), \underline{\xi}(t))} \quad [\text{USD/MWh}] \quad (9a)$$

$$\text{subject to} \quad \underline{z}_{p,\text{lb}} \leq \underline{z}_p \leq \underline{z}_{p,\text{ub}} \quad (9b)$$

$$\underline{u}_{\text{lb}} \leq \underline{u}(t) \leq \underline{u}_{\text{ub}} \quad (9c)$$

$$\underline{\xi}_{\text{lb}} \leq \underline{\xi}(t) \leq \underline{\xi}_{\text{ub}} \quad (9d)$$

$$0 \leq \sigma_{\text{base}}(t, \underline{z}_p, \underline{u}(t), \underline{\xi}(t)) \leq \sigma_{\text{base,ub}} \quad (9e)$$

$$0 \leq \sigma_{\text{top}}(t, \underline{z}_p, \underline{u}(t), \underline{\xi}(t)) \leq \sigma_{\text{top,ub}} \quad (9f)$$

$$\xi_3(t_0) = \hat{\xi}_3^{\text{op}} \quad (9g)$$

$$\underline{\zeta}(t) = \dot{\underline{\xi}}(t) - \{\hat{\mathbf{A}}(\underline{z})[\underline{\xi}(t) - \hat{\xi}^{\text{op}}(\underline{z})] + \hat{\mathbf{B}}(\underline{z})[\underline{u}(t) - \hat{\underline{u}}^{\text{op}}(\underline{z})]\} = \underline{0} \quad (9h)$$

$$\text{where} \quad \underline{z} = \begin{bmatrix} \underline{z}_p^T & v \end{bmatrix}^T \quad (9i)$$

$$\text{AEP}(\underline{z}_p^\dagger, \underline{u}^*(t), \underline{\xi}^*(t)) = 8760 \sum_{v=v_i}^{v_o} \left[P^*(\underline{z}_p^\dagger, \underline{u}^*(t), \underline{\xi}^*(t), v) f(v, \underline{z}_p^\dagger) \right]. \quad (9j)$$

The main objective is to minimize the LCOE (9a). LCOE depends on two primary components: Cost, which is solely a function of plant parameters in the model used here (as costs related to control scheme is not captured in the model), and AEP, which depends upon plant design variables and control and state trajectories.

The term $\text{Cost}(\underline{z}_p)$ in Eq. (9a) is evaluated with the Wind-plant Integrated System Design & Engineering

Model (WISDEM), an open source code developed and maintained by the NREL [63]. Starting from WISDEM input for the IEA 15 MW reference turbine as a baseline, WISDEM's component-wise cost and scaling model (CSM) translate each candidate FOWT design into detailed capital and operating cost estimates. The design variables, including dimensions, are passed directly to the subsystem models, which update component and material masses and costs. Furthermore, approximations for balance of station cost, operational and maintenance costs based on the provided turbine design are also provided. The WISDEM CSM estimates use simple regressions based on theories and scaling studies [64–67]. A full description of WISDEM's cost formulations is beyond the scope of this paper. The reader is referred to the model documentation [68] for further detail.

The optimization process must satisfy variable bounds on plant design variables (9b), path and boundary constraints on control and system state trajectories (9c, 9d, and 9g), and path constraints on the tower top and bottom stresses (9e and 9f). The initial value of the third state, $\xi_3(t) = \omega(t)$, is obtained from the DFSM using the ROSCO controller [26], and the system dynamics are governed by a defect constraint, $\zeta(t) = 0$ (9h). This defect constraint enforces the DFSM-based dynamic governing equation given in Eq. (4) over the entire time horizon. This constraint depends both upon design variables and wind speed (9i). To calculate the AEP, the optimal output power P must be determined for the 11 distinct wind profiles shown in Fig. 7 and summed, taking into account the corresponding PDFs (9j).

We employ a nested CCD approach. In the outer loop, we update plant design parameters and compute the Cost, while in the inner loop, we maximize AEP, thereby minimizing LCOE for the current plant configuration. Specifically, the inner loop maximizes the time-averaged output power across 11 distinct wind speeds in a 600-second simulation, subject to the constraints. These profiles cover the entire Region 2 and Region 3 operating envelope. A 600 s time horizon is (i) sufficiently long to capture continuous transient behavior while minimizing impact of numerical instabilities and settling transients, yet (ii) short enough to be evaluated hundreds of times within the optimization loop, a duration commonly adopted in transient wind-turbine studies. Given that these 11 independent 600 s wind profiles each represent a wind-speed bin of Weibull probabilistic distribution, weighting their time-averaged power outputs by these probabilities yields an unbiased, computationally efficient estimate of AEP. The same weighted sum constitutes the denominator of the outer-loop LCOE objective, ensuring full consistency between the inner-loop maximization and the outer-loop minimization. The inner-loop objective function is:

$$P = \frac{1}{t_f - t_0} \int_{t_0}^{t_f} \left(P(t) - 10^{-7} \dot{u}_1^2(t) - 10^7 \dot{u}_2^2(t) \right) dt, \quad (10)$$

where P is the time-averaged power for each wind speed v shown in Fig. 7(a). The variables u_1 and u_2 denote the control signals (generator torque and blade pitch), respectively, while \dot{u}_1 and \dot{u}_2 are their time derivatives. The third and fourth terms of the integrand form a penalty function that addresses singular arc issues. These penalty terms were calibrated by testing different values that yielded good performance of the OLOC solver while keeping each penalty term at least four orders of magnitude smaller than the nominal power P , ensuring the penalties do not dominate the objective. The superscript asterisk (*) denotes the optimal solution and dagger (†) denotes the current solution candidate in the optimization loop.

3.1. CCD Procedures

The CCD methodology in this study involves two-stages: the first (ROSCO) stage employs a simultaneous CCD formulation illustrated in Fig. 8, while the second (OLOC) stage begins near the optimal plant design identified by the ROSCO stage and uses a nested CCD formulation illustrated in Fig. 9. The superscript asterisk (*) denotes the optimal solution, dagger (†) denotes the current solution candidate in

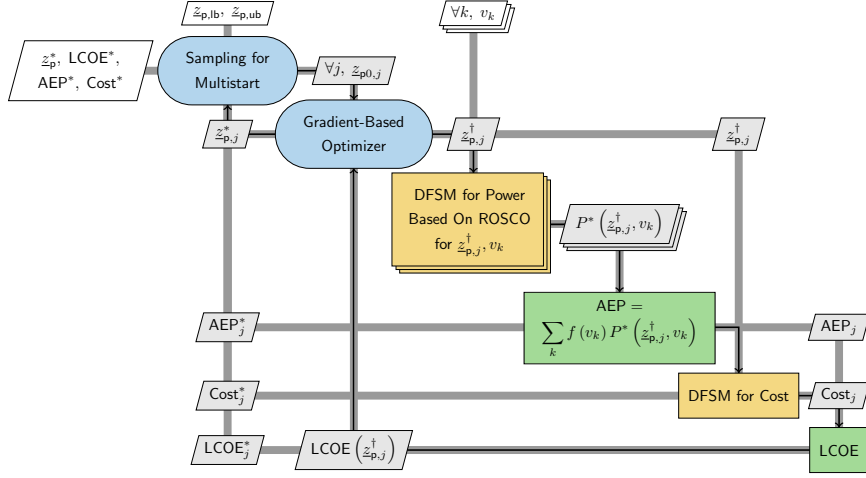


Figure 8: First (ROSCO) stage of the two-stage CCD optimization process, where DFSM predicts ROSCO controller responses to compute AEP.

the outer-loop optimization, and double dagger (\ddagger) denotes the current solution candidate in the inner-loop optimization problem.

In the ROSCO stage illustrated in Fig. 8, the DFSM trained with the ROSCO controller responses is used to determine the optimal plant design and control scheme that minimizes LCOE. During this stage the ROSCO controller parameters remain fixed to the reference turbine specification. This stage serves only to generate the initial plant design points passed to the OLOC stage optimization problem. Specifically, the plant design vector z_p is updated within the feasible region that satisfies the tower stress constraint, and the power outputs for given wind profiles, which are required to compute AEP, are also determined by the trained DFSM. Once convergence is reached, the optimal plant design z_p^* is obtained along with the corresponding LCOE*, AEP*, and Cost* values. The 40 initial guesses are generated by a space-filling sampling procedure (see “sampling for multistart” block in Fig. 8), which scatters starting point for gradient-based optimizer across feasible region and increases the chance of locating the global optimum. The solution to the problem of this stage (see “gradient-based optimizer” block and elements underneath) fed to the second (OLOC) stage. Optimizing plant design variable subject to dynamic constraints inherently achieve co-design of plant and control scheme without spending significant computational expenses since the DFSM is trained to emulate the behavior of ROSCO. This first stage leverages this computational advantage in exploring global design space. To be specific, the optimal plant design obtained in this stage corresponds to the best plant in the context of requiring use of ROSCO. However, this optimal plant design does not guarantee the optimality when optimized with OLOC due to greater control signal flexibility. Notably, using DFSM at this stage allows all 40 initial guesses to be optimized in under 10 minutes.

In the OLOC stage, shown in Fig. 9, we adopted a nested CCD formulation. The outer-loop (Fig. 9(a)) mirrors the problem structure of the ROSCO stage, but its “Power” block now calls an inner-loop optimal-control problem instead of calling the ROSCO-based DFSM. This inner loop (Fig. 9(b)) solves an OLOC problem with the DFSM dynamics, given in Eq. (4). For each wind profile v_k , the inner-loop returns optimal state (simulation results) and control (optimal solution) trajectories, and time-averaged power passed to outer-loop problem to compute AEP using Weibull distribution, which in turn is used to calculate LCOE, the outer-loop objective function. Among all optimized solutions, the design delivering the lowest LCOE is selected as the final optimal solution. The use of OLOC enables to fully exploit the dynamic regulations

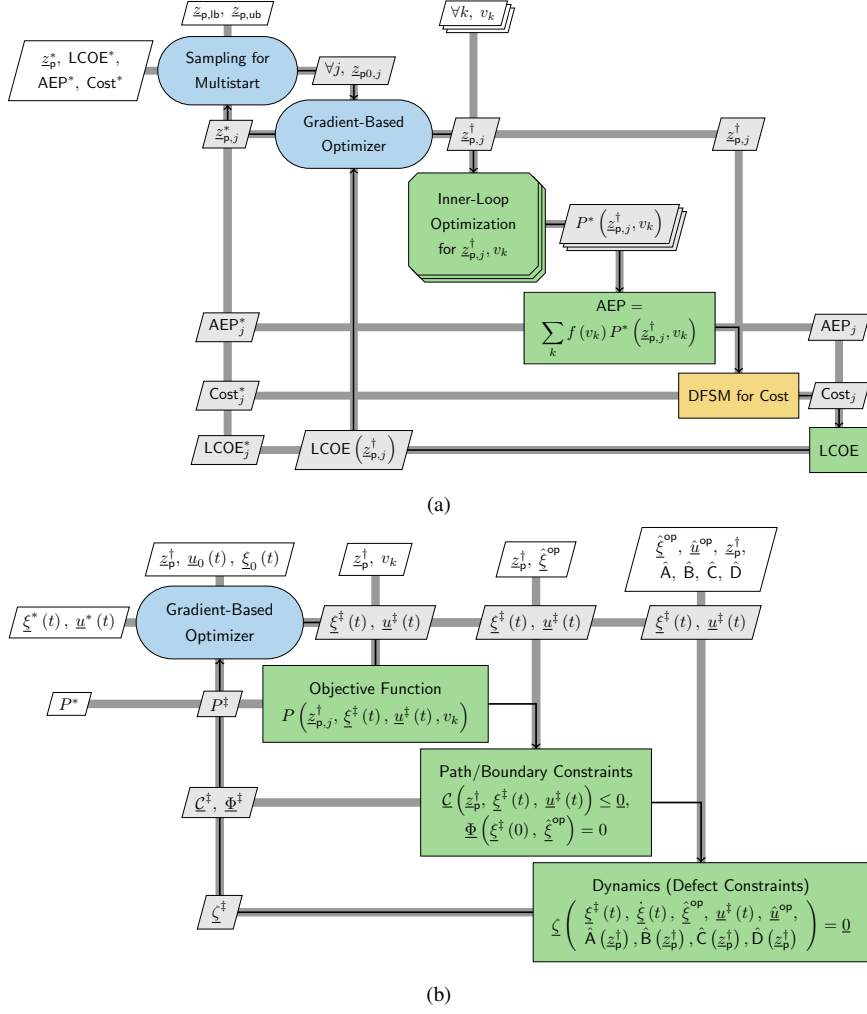


Figure 9: Second (OLOC) stage of the two-stage CCD optimization process: (a) Outer-loop optimization problem, and (b) Inner-loop optimization problem that fully utilizes OLOC’s flexibility.

beyond what ROSCO can provide. While the dynamic response is provided by the trained DFSM, the control signal regulation is provided fully independently via OLOC solver in the inner-loop problem.

4. Results

This section presents the outcomes of several design optimization scenarios and control design methods applied to the overall wind turbine system. The analysis of these studies focuses on comparing different design strategies and their influence on key performance metrics and parameters. In addition, optimal design results are further analyzed through sensitivity studies, and comparison of control design approaches.

4.1. Results of Various Optimization Scenarios and Cases

In this section, we examine three distinct optimization approaches: (1) *Baseline*, (2) *Sequential*, and (3) *CCD* scenarios. In the *Baseline* scenario, the plant design remains fixed at the IEA 15 MW reference turbine specification, after which either a single ROSCO stage or a two-stage ROSCO–OLOC approach

Table 1: Comparison of three design strategies (*Baseline*, *Sequential*, and *CCD*) and two control design strategies (ROSCO and OLOC) under varying tower stress constraints (80–120 MPa).

Scenario / Constr. (MPa)	Control	LCOE	AEP	Cost	l_{hub}	D_{top}	b_{base}	b_{top}	D_{rotor}
<i>Baseline</i> ($\sigma \leq 103$)	ROSCO	86.97	74.97	65.20	150.0	6.50	0.041	0.021	240.0
	OLOC	84.72	76.96	65.20	150.0	6.50	0.041	0.021	240.0
<i>Sequential</i> : $\sigma \leq 103$	ROSCO	86.40	75.14	64.92	155.0	5.88	0.029	0.025	240.0
	OLOC	84.39	76.93	64.92	155.0	5.88	0.029	0.025	240.0
<i>CCD</i> : $\sigma \leq 80$	ROSCO	86.99	75.19	65.41	155.0	6.72	0.036	0.025	240.0
	OLOC	84.74	77.13	65.36	155.0	6.79	0.037	0.025	240.0
<i>CCD</i> : $\sigma \leq 103$	ROSCO	86.40	75.14	64.92	155.0	5.88	0.029	0.025	240.0
	OLOC	84.15	77.23	64.99	155.0	6.09	0.031	0.024	240.0
<i>CCD</i> : $\sigma \leq 120$	ROSCO	86.24	75.12	64.71	155.0	5.43	0.025	0.025	240.0
	OLOC	83.85	77.26	64.79	155.0	5.63	0.027	0.025	240.0

(hereafter “OLOC”) is applied for control design (see Sect. 3.1 for details). In the *Sequential* scenario, the plant design is first optimized to minimize LCOE using the DFSM trained with ROSCO controller responses, followed by a subsequent optimization using either the ROSCO or OLOC control design. Finally in the *CCD* scenario, both plant and control designs are optimized concurrently via either the “ROSCO” or “OLOC” CCD approach, as illustrated in Figs. 8 and 9, respectively.

Table 1 summarizes the results of various scenarios, while Fig. 10 offers a visual comparison. All data are normalized with respect to the *Baseline* ROSCO case. The *CCD* scenarios focus on the influence of different maximum tower stress constraints on design outcomes and their performances. In this study, von Mises stress constraints computed using all force and moment components are employed at the top and base sections of the tower. The maximum allowable tower stress is set to 80, 103, or 120 MPa. In the *Baseline* ROSCO case, where the ROSCO controller response was used, the maximum tower stress reached 103 MPa. Consequently, this work investigates how the design changes when the tower stress constraint is tightened to 80 MPa or relaxed to 120 MPa.

Figure 10(a) illustrates the relative values of AEP, Cost, and LCOE compared to those of *Baseline* ROSCO case. Figure 10(b) presents the relative changes in plant design variables with respect to the same baseline case. The OLOC cases are represented by square symbols connected with solid lines, while the ROSCO cases are depicted by dots connected with dash-dotted lines.

In every scenario, the OLOC cases consistently produce a lower LCOE, and higher AEP compared to the ROSCO cases. This outcome is expected because ROSCO functions as a CLC with limited tunability, whereas OLOC can freely adjust the control trajectories, provided that the constraints and system dynamics are satisfied. Despite a consistent decrease in LCOE and an increase in AEP, the overall cost does not necessarily decrease. As shown in Fig. 10(a), in the last two CCD cases, the cost of the OLOC designs is actually higher than that of the ROSCO cases. This is due to the fact that, as illustrated in Fig. 10(b), the OLOC results feature larger tower base thicknesses and tower-top diameters. However, the key insight is that although the cost is slightly higher in these OLOC cases, the resulting LCOE is still lower. This demonstrates the benefit of using OLOC: by fully leveraging the coupling between plant and controller design, the AEP is significantly improved, while the increase in cost remains relatively small. As a result, the LCOE is reduced, highlighting one of the key advantages of using OLOC in CCD to fully capitalize on the potential of plant-controller co-design.

Under the consistent maximum tower stress constraint ($\sigma \leq 103$ MPa), the *CCD* scenario achieves the

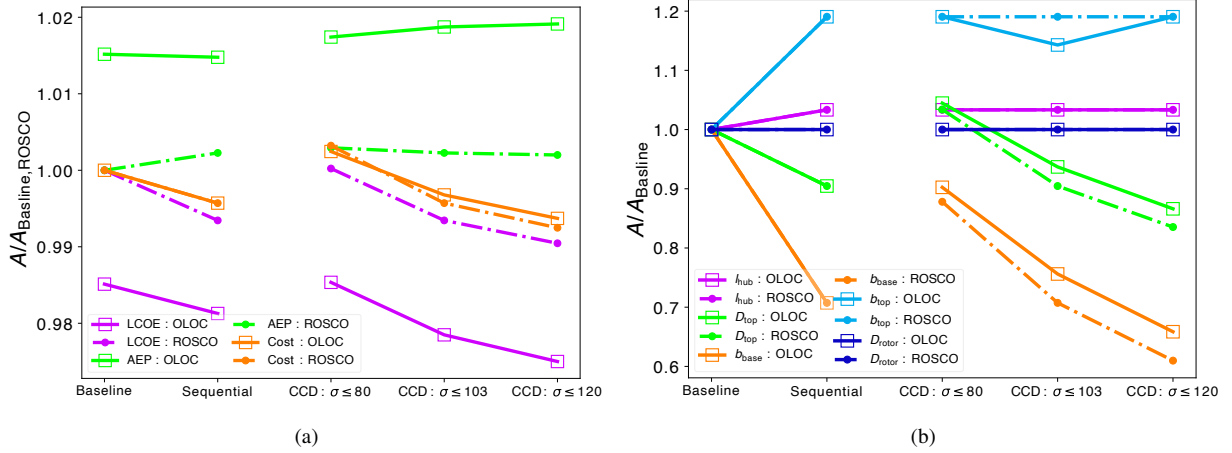


Figure 10: Impact of optimization workflow (Sequential, CCD) and control design strategies (ROSCO, OLOC) on performance and plant design. All quantities are normalized to the *Baseline ROSCO* case to highlight relative changes. (a) AEP, Cost, and LCOE comparison for five scenarios: *Baseline*, *Sequential*, and *CCD* with varied tower stress constraints. Dot symbols with dash-dotted lines denote ROSCO, while square symbols with solid lines denote OLOC. (b) Key plant design variables compared for the same five scenarios, using the same symbols and lines.

lowest LCOE, followed by the *Sequential* and then the *Baseline* scenario. This trend holds for both ROSCO and OLOC control design cases, and can be attributed to the fact that *CCD* scenario concurrently optimizes the plant and control designs, exploiting their co-design synergy, while the *Sequential* scenario optimizes both elements separately, without leveraging the full benefits of co-design.

In the *CCD* scenarios, relaxing the maximum allowable tower stress from 103 MPa to 120 MPa further reduces LCOE. The optimized plant designs incorporate smaller tower diameters and thinner tower walls, thereby lowering overall costs. These findings highlight the profound influence of tower stress limits on *CCD* optimization, underscoring the importance of such constraints in wind turbine design.

Furthermore, in all examined cases, except for the *Baseline* scenario, where the plant design is fixed, both the hub height and rotor diameter reach their upper bounds. This outcome arises because a larger rotor diameter increases aerodynamic torque, enabling higher power generation, and increasing the hub height shifts the Weibull distribution toward greater AEP. This result aligns closely with the sensitivities shown in Fig. 4, where tower length and rotor diameter exert the strongest influence on the Cost/Power metric. Although here the optimal design for these two variables converges to their upper bounds, if the ranges of these design variables were expanded or additional constraints (e.g., buckling) were incorporated in future studies, these parameters might not always reach their upper bounds. As this study serves as a preliminary exploration, it does not encompass the full spectrum of potential constraints.

Finally, to satisfy the tower stress constraints at the tower top section, two key parameters: tower top diameter (D_{top}) and tower top thickness (b_{top}), are primarily adjusted during optimization. The results show a tendency to increase the top thickness of the tower first, as it is generally less expensive than enlarging the tower diameter. Only if necessary does the design expand the diameter of the tower. This result is also consistent with the sensitivities shown in Fig. 4, where, between b_{top} and D_{top} , the sensitivity of b_{top} on σ_{top} is about half that of D_{top} , while its sensitivity to Cost is only about one-fifth of that of D_{top} . Meanwhile, to satisfy the tower stress constraints at the base, the tower base diameter is fixed at 10 m, so the wall thickness is adjusted accordingly to minimize LCOE while still meeting stress-related design requirements.

Figure 11 presents tower designs for various design optimization scenarios, including zoomed-in views

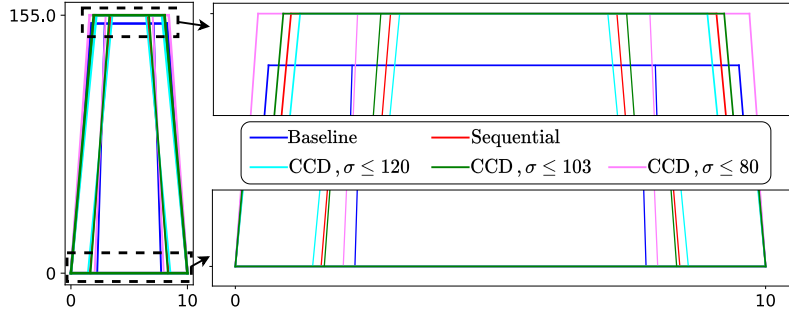


Figure 11: Side view of optimal tower geometry evolution across varied design scenarios. Solid profiles show the outer and inner diameters of the tower for five optimized designs: *Baseline*, *Sequential*, and *CCD* with varied tower stress constraints. All optimized towers (except *Baseline*) approach the upper height limit to maximize energy production. Tighter stress constraint leads to thicker tower section and larger diameters.

of the top and bottom sections. Notably, tower designs from all cases except the baseline reach the upper bound of tower height. Additionally, reducing the maximum allowable tower stress (tightening the stress constraints) results in towers with larger outer diameters and thicker base and top sections.

Compared with the sequential design process, CCD fully leverages OLOC’s ability to reshape rotor torque and tower-top moments during the design search. Because the controller is optimized together with the plant, it can actively attenuate peak fore-aft loads, allowing the optimizer to trade off wall thickness against more aggressive control actions to maximize power, while satisfying the prescribed stress concentrations, as shown in Fig. 10(b). Sequential design lacks this synergy. The tower is sized with limited knowledge and fixed controller first, so the tower thickness cannot be relaxed accounting for the possibility of aggressive control in attenuating fore-aft loads. This cooperative load-sharing mechanism explains the observed cost gap and highlights the unique benefit of simultaneous plant and controller co-design.

4.2. Sensitivity Study

It is important to understand how a change to one plant design variable affects other design variables and performance metrics. The sensitivity analysis presented here helps us understand the interdependencies and impacts among these variables. An optimal design obtained from the *CCD-ROSCO* case with a maximum stress constraint of 103 MPa is selected for sensitivity analysis, as detailed in Tab. 2. In each column of the table, one plant design variable is adjusted from its optimal value by approximately 10% of its range. Then, the resulting changes in the optimal values of the other four plant design variables and performance metrics, such as AEP, Cost, and LCOE, are presented.

Each entry at row i and column j reports the percentage change in the quantity listed in row i caused by a small percentage perturbation in the design variable in column j . For every column, we computed:

$$S_{ij} = \frac{\frac{y_i(\underline{z}_p^j) - y_i(\underline{z}_p)}{y_i(\underline{z}_p)}}{\frac{\underline{z}_p^j - \underline{z}_p}{\underline{z}_p}} \times 100\%, \quad (11)$$

where \underline{z}_p is the baseline vector of five plant design variables, \underline{z}_p^j is the same vector with a small perturbation applied to its j -th component, and y_i is the variable or performance metric in the i -th row. This normalization removes bias from differences in absolute scale, ensuring fair comparison between variables with different

Table 2: Sensitivity analysis of wind turbine plant design variables, demonstrating their interdependencies.

	l_{hub}	D_{top}	b_{base}	b_{top}	D_{rotor}
l_{hub}		0^+	0^+	0^+	0^+
D_{top}	0.44		-0.18	-55.97	-160.12
b_{base}	148.55	0.58		0^+	112.33
b_{top}	0^+	-151.4	0^+		355.68
D_{rotor}	0^+	0^+	0^+	0^+	
LCOE	-6.59	1.29	0.60	-0.73	-83.20
AEP	10.98	-0.26	0.06	0.299	89.80
Cost	4.78	0.99	0.65	-0.58	7.40

scales. The sign of S_{ij} indicates the direction of influence, while its magnitude measures the coupling strength. A value of 0^+ means the row variable has already reached its upper bound, and therefore does not respond to the perturbation. A concrete example clarifies the table’s meaning: the entry -160.12 in the second row, last column of Tab. 2 implies that a $\pm 10\%$ change in rotor diameter D_{rotor} induces a $\mp 16.0\%$ change in tower-top diameter D_{top} , because $-160.12 \times 10\% = -16.01\%$.

As shown in Tab. 2, the analysis demonstrates that both hub height (l_{hub}) and rotor diameter (D_{rotor}) significantly influence LCOE. Increasing these parameters leads to higher AEP, as the additional energy production offsets the increased Cost associated with taller and thicker towers, thereby reducing overall LCOE. Additionally, increasing the tower top thickness (b_{top}) results in a small decrease in LCOE. This reduction is achieved by decreasing the tower top diameter (D_{top}) while maintaining compliance with stress constraints of the tower. Consequently, the total Cost decreases, and there is a marginal increase in AEP. This trend aligns with the CCD results presented in Tab. 1, where b_{top} generally converges toward its upper bound.

Moreover, there is a strong correlation between D_{rotor} and other parameters, including D_{top} , b_{base} , and b_{top} . As D_{rotor} increases, the tower must become thicker to satisfy stress constraints. At the tower base, where the diameter is fixed at 10 m, only the thickness (b_{base}) can be adjusted. At the tower top, both b_{top} and D_{top} can be adjusted. The results indicate a preference for increasing b_{top} first, as this is generally less costly than increasing D_{top} . Consequently, D_{top} decreases while b_{top} and b_{base} increase. It is important to note that if the ranges of these design variables were expanded or additional constraints (e.g., buckling) were considered in future studies, these parameters might not reach their upper bounds.

Lastly, Tab. 2 shows that raising l_{hub} , b_{top} , and D_{rotor} lowers LCOE. One might therefore wonder why the CCD-ROSCO case with $\sigma \leq 103$ MPa in Tab. 1 did not converge to larger values of these variables for achieving better LCOE. The reason is that all three had already reached their prescribed upper bounds. Expanding those bounds or adding additional, more realistic, constraints would widen the design space and permit exploration of alternative configurations that remain structurally feasible. These sensitivity results are presented to provide a more comprehensive understanding and explore potential interactions among the design variables. Although this study used the CCD case with a maximum stress limit of 103 MPa, different cases or the introduction of more realistic constraints are expected to produce varying design outcomes accordingly.

Figure 12 illustrates the LCOE, Cost, and AEP performance responses, alongside tower stress levels, across the design space for tower top thickness (b_{top}) and tower top diameter (D_{top}). Figure 13 presents the same performance responses and tower stress levels across the design space for tower base thickness (b_{base}) and hub height (l_{hub}). In these figures, dotted lines represent stress isolines, while solid lines denote iso-

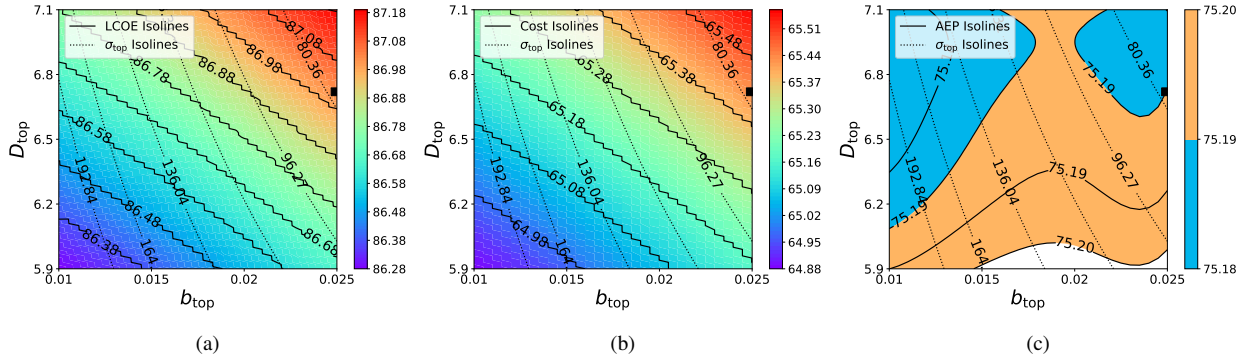


Figure 12: Effect of tower top geometry variable subspace (b_{top} and D_{top}) on key performance metrics (LCOE, Cost, and AEP). All other plant design variables are fixed. Black square marker represents the ROSCO stage optimal solution. Dotted lines represent stress isolines, while solid lines denote isolines for each performance metric. (a) LCOE, (b) Cost, (c) AEP contours.

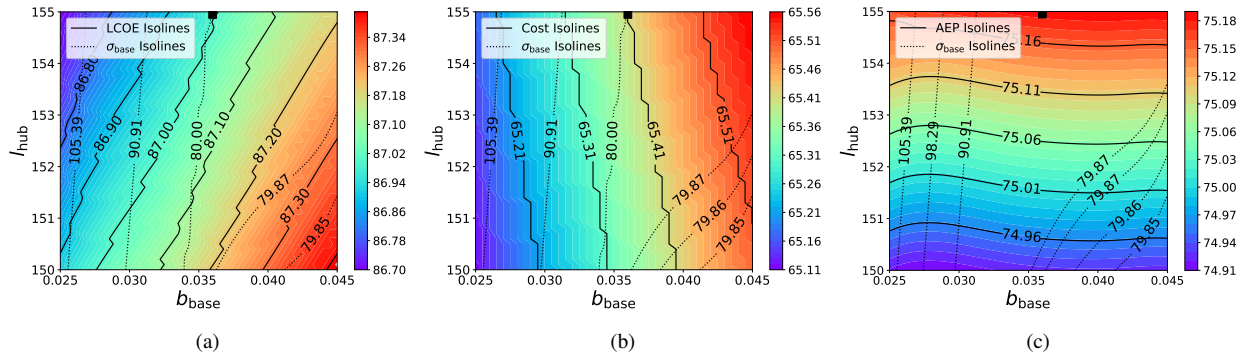


Figure 13: Effect of tower base wall thickness and hub height variable subspace (b_{base} and l_{hub}) on key performance metrics (LCOE, Cost, and AEP). All other plant design variables are fixed. Black square marker represents the ROSCO stage optimal solution. Dotted lines represent stress isolines, while solid lines denote isolines for each performance metric. (a) LCOE, (b) Cost, (c) AEP contours.

lines for each performance metric. The black square marker highlights the optimal CCD solution achieved through ROSCO control strategy. In these plots, design space variables (b_{top} and D_{top} for Fig. 12; b_{base} and l_{hub} for Fig. 13) are varied within defined ranges, while other plant parameters are fixed at the CCD case design solution with a maximum stress constraint of 80MPa, as detailed in Tab. 1.

Variations in tower top thickness (b_{top}) and tower top diameter (D_{top}) have ignorable amount of impact on AEP, and even this small impact is likely due to inherent simulation noise generated by OpenFAST. However, these parameters significantly influence stress, Cost, and LCOE. The optimal solution (indicated by the black square marker) resides within a region where the maximum tower stress constraint of 80 MPa is satisfied and LCOE is minimized. Increasing the maximum allowable tower stress allows for a reduction in LCOE by employing thinner tower walls.

The wiggles in the LCOE and Cost isolines in Figs. 12 and 13 arise from noisy, partly discrete, low-sensitivity nature of the WISDEM cost model, which introduces step changes in the cost estimate and produces locally non-monotonic variations. For example, as shown in Fig. 12(b), when the tower-top diameter is held constant, small changes in tower wall thickness (x -axis) yield only minor variations in Cost. Conversely, slight variations in tower diameter can trigger a sudden jump in Cost because of the discrete sizing of internal components and parts. In contrast, the AEP isolines remain smooth because they depend

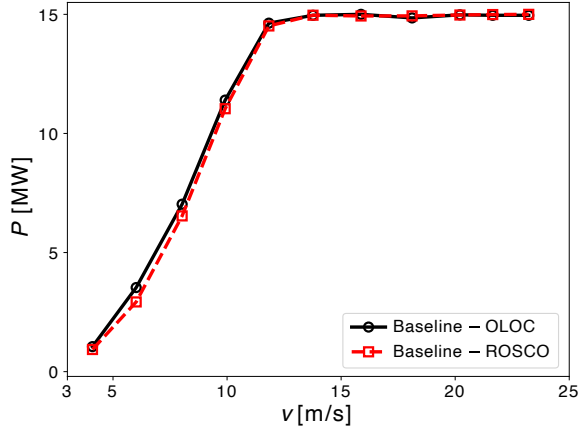


Figure 14: Comparison of power curves for the baseline tower using OLOC (solid line) and ROSCO (dashed line).

continuously on aerodynamic and structural physics. Although Cost and, therefore, LCOE exhibits minor wiggles, their impact on the overall trend and on the effectiveness of gradient-based optimizers is negligible.

4.3. ROSCO vs OLOC Comparison

As presented in Tab. 1, the OLOC design approach demonstrates a notable reduction in LCOE and an increase in AEP compared to the ROSCO controller-based approach. The observed enhancement in AEP can be attributed to the ability of OLOC to modify the power curve derived from DFSM. Figure 14 illustrates the power curves for the baseline tower, comparing the results obtained using OLOC and ROSCO under identical constraints. Notably, the power curve generated by OLOC consistently outperforms that of ROSCO. Specifically, as shown in the first two rows of Tab. 1, the application of OLOC increases AEP from 74.97 to 76.96 MWh. Since the Cost remains unchanged between the two cases, this improvement in AEP translates directly to a reduction in LCOE from 86.97 to 84.72 USD/MWh.

The observed increase in power output and, consequently, the AEP, can be attributed to the control strategies and corresponding system states at different wind speeds, as depicted in Fig. 7. Figure 15 demonstrates the performance of the baseline tower under four distinct DLCs, comparing the results achieved with the OLOC- and ROSCO-based control strategies. In this figure, the outcomes from the OLOC simulation are represented by thick solid lines, while those from the ROSCO controller are depicted as thin solid lines.

Figure 15 compares the OLOC and ROSCO control strategies on wind turbine performance under varying wind speeds. The bold solid lines represent results obtained using the OLOC control strategy, while the thin lines present results from the ROSCO control strategy. This figure demonstrates the impact of different controllers on turbine performance in varying wind conditions.

In Fig. 15(a), the rotor rotational velocity (ω) time histories are plotted. Initially, both the OLOC and ROSCO scenarios start with the same values, corresponding to the nominal steady-state value obtained by OpenFAST linearization. However, over time, ROSCO tends to maintain a higher rotational velocity compared to OLOC's regulation, primarily due to CLC's limitations in satisfying path constraints. Figure 15(b) displays the generator torque (T_{gen}), where the OLOC results maintain slightly higher values. Figure 15(c) illustrates the collective blade pitch angle (β), showing that the two control approaches do not exhibit significant differences in blade pitch control. In Fig. 15(d), the normalized generator output power ($P_{gen}/15$ MW) is depicted. Here, the OLOC scenario exhibits slightly higher power levels, leading to higher AEP compared to the ROSCO scenario. As observed, the increased power achieved via the OLOC strategy is accompanied

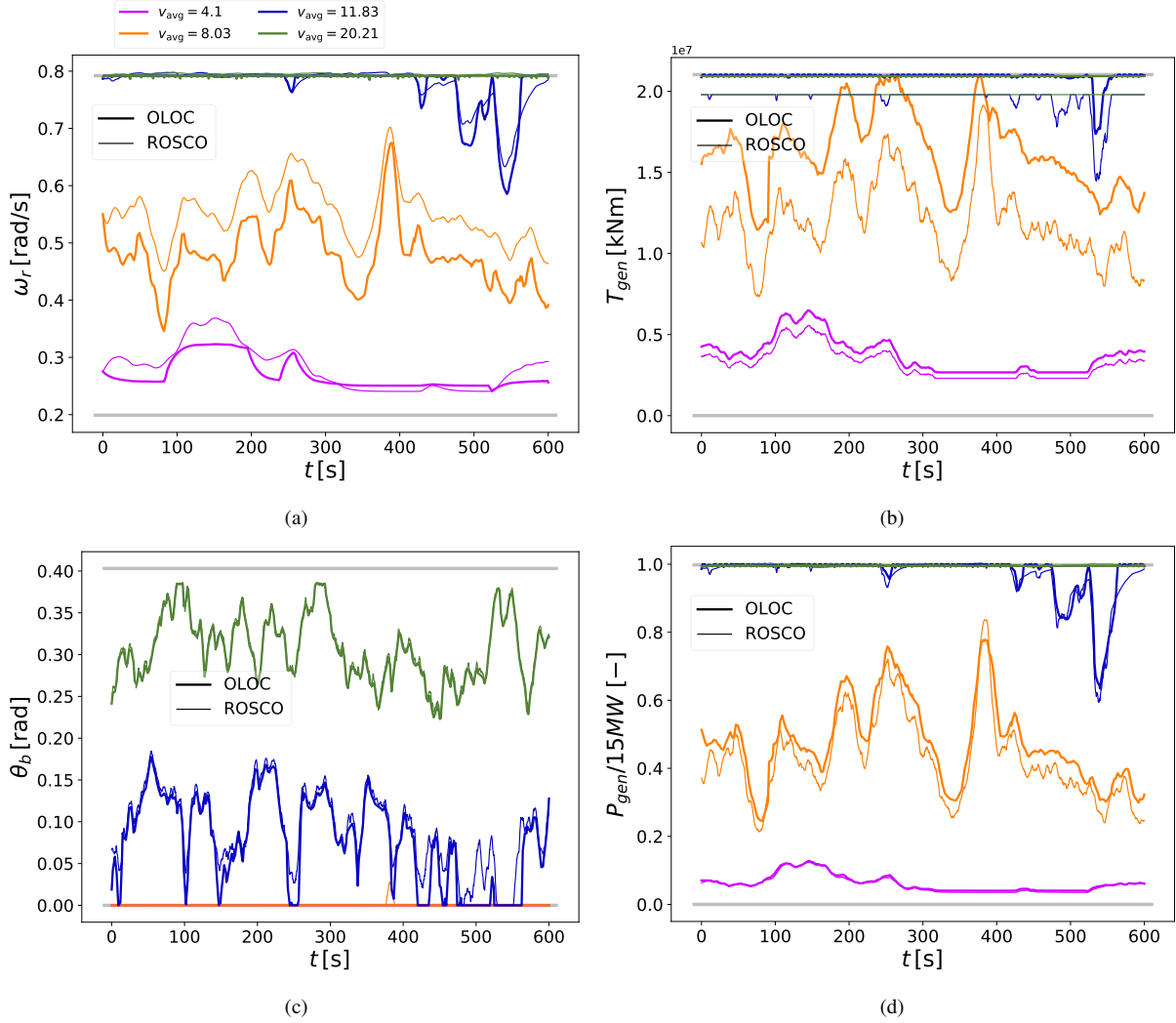


Figure 15: Comparison of OLOC and ROSCO control strategies on wind turbine performance under varying wind speeds. (a) Rotor rotational velocity (ω). (b) Generator torque (T_{gen}). (c) Blade pitch angle (β). (d) Normalized generator power output (P_{gen}).

by slightly higher generator torque and lower rotor speed compared to the ROSCO CLC approach.

5. Conclusion

This article introduces a comprehensive CCD framework for wind turbine systems, leveraging nonlinear DFSMs developed through OpenFAST linearization and data-driven approaches. The developed DFSMs provide state derivatives ($\dot{\xi}$) and system output responses (y) across a wide range of plant and control design parameters, and they are validated against direct simulation responses. The research findings demonstrate that the CCD approach offers substantial benefits over traditional *Sequential* methodologies by exploiting the co-design synergies between plant and control domains. Notably, the proposed CCD framework enables a significant reduction in LCOE by finding optimally balancing enhancements in AEP and reductions Cost, while satisfying constraints related to design and physical limits, as well as dynamic governing equations.

Key results highlight the superior performance of the OLOC-based CCD optimization compared to CLC based on ROSCO. This superiority is driven by OLOC's ability to dynamically adjust control trajectories and leverage plant-control synergies. The framework successfully balances competing objectives, such as cost associated with plant design parameters, energy production across various wind profiles, and structural integrity under varying stress constraints. These findings underscore the critical role of tower stress limits in guiding design trade-offs.

The sensitivity analysis reveals interdependencies among design variables and performance metrics. Specifically, hub height (l_{hub}) and rotor diameter (D_{rotor}) have a pivotal influence on AEP, leading to lower LCOE. Additionally, the study highlights nuanced interactions between various parameters. Increasing tower top thickness (b_{top}) results in reduced optimal tower top diameter (D_{top}) while maintaining compliance with stress constraints (σ_{base} and σ_{top}), ultimately lowering Cost. These interdependencies provide valuable guidance for exploring design trade-offs in future studies and demonstrate the essential role of such analyses in refining the optimization process.

Another significant contribution of this study is the sparsity analysis, which offers valuable insights into the relationships between input variables (such as states, controls, and wind speed) and output variables (including system responses, state derivatives, and tower stresses), ultimately linking them to design variables. The analysis highlights the relative importance of each input variable in shaping specific system responses, thereby guiding critical areas of focus in the optimization process. It reveals that blade pitch angle and generator torque significantly influence key outputs, such as aerodynamic force, aerodynamic torque, and side-to-side moments. Additionally, certain outputs, such as fore-aft motion and aerodynamic moments, are highly sensitive to certain inputs, such as wind speed and blade pitch angle. Notably, the fore-aft moment emerged as the dominant contributor to tower stresses at both the top and base sections. These findings emphasize the importance of identifying influential relationships, enabling targeted adjustments and refined CCD problem formulation.

As the findings of this study are intended for the early-stage exploration phase of wind turbine development, subsequent research focused on later-stage development should broaden the scope of constraints, incorporate higher-fidelity models, and utilize comprehensive and tailored sets of DLCs to better address complex, real-world scenarios. Expanding parameter bounds and integrating additional design considerations, such as buckling constraints, will offer deeper insights into the practical applications and limitations of the CCD framework. By establishing a robust foundation for wind turbine design, this study highlights the significant potential of CCD to drive system-level optimization and innovation in renewable energy systems.

CRedit authorship contribution statement

Yong Hoon Lee: Writing – original draft, Writing - review & editing, Methodology, Conceptualization, Investigation, Visualization, Project administration. **Saeid Bayat:** Writing – original draft, Writing - review & editing, Methodology, Investigation, Data curation, Validation, Visualization. **James T. Allison:** Writing - review & editing, Supervision, Project administration, Funding acquisition.

Declaration of Competing Interest

The authors declare that they have no competing interests.

Acknowledgment

The information, data, or work presented herein was funded in part by the U.S. Department of Energy, Advanced Research Projects Agency-Energy (ARPA-E) under grant number DE-AR-0001766. The authors would like to thank Sunil Tamang for his valuable assistance with reviewing and visualization, which contributed significantly to the completion of this paper.

References

- [1] L. Y. Pao, D. S. Zalkind, D. T. Griffith, et al., Control co-design of 13 MW downwind two-bladed rotors to achieve 25% reduction in levelized cost of wind energy, *Annual Reviews in Control* 51 (2021) 331–343. doi:10.1016/j.arcontrol.2021.02.001.
- [2] P. Veers, C. L. Bottasso, L. Manuel, et al., Grand challenges in the design, manufacture, and operation of future wind turbine systems, *Wind Energy Science* 8 (2023) 1071–1131. doi:10.5194/wes-8-1071-2023.
- [3] S. Bayat, Y. H. Lee, J. T. Allison, Nested control co-design of a spar buoy horizontal-axis floating offshore wind turbine, *Ocean Engineering* 328 (2025) 121037.
- [4] A. K. Sundarrajan, Y. H. Lee, J. T. Allison, D. R. Herber, Open-loop control co-design of semisubmersible floating offshore wind turbines using linear parameter-varying models, *Journal of Mechanical Design* 146 (2024) 041704. doi:10.1115/1.4063969.
- [5] Y. H. Lee, S. Bayat, J. T. Allison, M. S. Hossain, D. T. Griffith, Multidisciplinary modeling and control co-design of a floating offshore vertical-axis wind turbine system, *Journal of Mechanical Design* (2025) 1–12.
- [6] M. Garcia-Sanz, Engineering microgrids with control co-design: principles, methods, and metrics, *IEEE Electrification Magazine* 9 (2021) 8–17. doi:10.1109/MELE.2021.3093595.
- [7] M. Garcia-Sanz, Control co-design: An engineering game changer, *Advanced Control for Applications* 1 (2019) e18. doi:10.1002/adc2.18.
- [8] H. K. Fathy, P. Y. Papalambros, A. G. Ulsoy, D. Hrovat, Nested plant/controller optimization with application to combined passive/active automotive suspensions, in: *American Control Conference*, volume 4, Denver, CO, USA, 2003, pp. 3375–3380. doi:10.1109/ACC.2003.1244053.
- [9] J. T. Allison, T. Guo, Z. Han, Co-Design of an Active Suspension Using Simultaneous Dynamic Optimization, *Journal of Mechanical Design* 136 (2014) 081003. doi:10.1115/1.4027335.
- [10] L. Y. Pao, M. Pusch, D. S. Zalkind, Control co-design of wind turbines, *Annual Review of Control, Robotics, and Autonomous Systems* 7 (2024) 201–226. doi:10.1146/annurev-control-061423-101708.
- [11] C. Santoni, A. Khosronejad, P. Seiler, F. Sotiropoulos, Toward control co-design of utility-scale wind turbines: Collective vs. individual blade pitch control, *Energy Reports* 9 (2023) 793–806. doi:10.1016/j.egyrs.2022.12.041.

- [12] M. Hall, S. Housner, D. Zalkind, et al., An open-source frequency-domain model for floating wind turbine design optimization, *Journal of Physics: Conference Series* 2265 (2022) 042020. doi:10.1088/1742-6596/2265/4/042020.
- [13] J. M. Hegseth, E. E. Bachynski, J. R. R. A. Martins, Integrated design optimization of spar floating wind turbines, *Marine Structures* 72 (2020) 102771. doi:10.1016/j.marstruc.2020.102771.
- [14] A. P. Deshmukh, J. T. Allison, Design of dynamic systems using surrogate models of derivative functions, *Journal of Mechanical Design* 139 (2017) 101402. doi:10.1115/1.4037407.
- [15] A. P. Deshmukh, J. T. Allison, Multidisciplinary dynamic optimization of horizontal axis wind turbine design, *Structural and Multidisciplinary Optimization* 53 (2016) 15–27. doi:10.1007/s00158-015-1308-y.
- [16] N. J. Abbas, J. Jasa, D. S. Zalkind, A. Wright, L. Y. Pao, Control co-design of a floating offshore wind turbine, *Applied Energy* 353 (2024) 122036. doi:10.1016/j.apenergy.2023.122036.
- [17] J. M. Hegseth, E. E. Bachynski, J. R. R. A. Martins, Design optimization of spar floating wind turbines considering different control strategies, *Journal of Physics: Conference Series* 1669 (2020) 012010. doi:10.1088/1742-6596/1669/1/012010.
- [18] N. J. Abbas, P. Bortolotti, C. Kelley, et al., Aero-servo-elastic co-optimization of large wind turbine blades with distributed aerodynamic control devices, *Wind Energy* 26 (2023) 763–785. doi:10.1002/we.2840.
- [19] A. P. Deshmukh, J. T. Allison, Unrestricted wind farm layout design with optimal control considerations, in: *ASME International Design Engineering Technical Conferences and Computers and Information in Engineering Conference*. Volume 2A: 43rd Design Automation Conference (DAC), DETC2017-67480, Cleveland, OH, USA, 2017, p. V02AT03A021. doi:10.1115/DETC2017-67480.
- [20] S. Raach, D. Schlipf, F. Sandner, D. Matha, P. W. Cheng, Nonlinear model predictive control of floating wind turbines with individual pitch control, in: *American Control Conference*, Portland, OR, USA, 2014, pp. 4434–4439. doi:10.1109/ACC.2014.6858718.
- [21] D. Schlipf, D. J. Schlipf, M. Kühn, Nonlinear model predictive control of wind turbines using lidar, *Wind Energy* 16 (2013) 1107–1129. doi:10.1002/we.1533.
- [22] O. El Beshbichi, Y. Xing, M. Chen Ong, Linear quadratic regulator optimal control of two-rotor wind turbine mounted on spar-type floating platform, *Journal of Offshore Mechanics and Arctic Engineering* 145 (2023) 022001. doi:10.1115/1.4055552.
- [23] L. Y. Pao, K. E. Johnson, A tutorial on the dynamics and control of wind turbines and wind farms, in: *American Control Conference*, St. Louis, MO, USA, 2009, pp. 2076–2089. doi:10.1109/ACC.2009.5160195.
- [24] M. Mirzaei, C. Tibaldi, M. H. Hansen, PI controller design of a wind turbine: evaluation of the pole-placement method and tuning using constrained optimization, *Journal of Physics: Conference Series* 753 (2016) 052026. doi:10.1088/1742-6596/753/5/052026.

- [25] H. Habibi, H. Rahimi Nohooji, I. Howard, Adaptive PID control of wind turbines for power regulation with unknown control direction and actuator faults, *IEEE Access* 6 (2018) 37464–37479. doi:10.1109/ACCESS.2018.2853090.
- [26] N. J. Abbas, D. S. Zalkind, L. Pao, A. Wright, A reference open-source controller for fixed and floating offshore wind turbines, *Wind Energy Science* 7 (2022) 53–73. doi:10.5194/wes-7-53-2022.
- [27] S. Bayat, J. T. Allison, Control co-design with varying available information applied to vehicle suspensions, in: *International Design Engineering Technical Conferences and Computers and Information in Engineering Conference*, volume 87301, American Society of Mechanical Engineers, 2023, p. V03AT03A002.
- [28] A. P. Deshmukh, D. R. Herber, J. T. Allison, Bridging the gap between open-loop and closed-loop control in co-design: A framework for complete optimal plant and control architecture design, in: *American Control Conference*, Chicago, IL, USA, 2015, pp. 4916–4922. doi:10.1109/ACC.2015.7172104.
- [29] E. Loth, C. Qin, J. G. Simpson, K. Dykes, Why we must move beyond LCOE for renewable energy design, *Advances in Applied Energy* 8 (2022) 100112. doi:10.1016/j.adapen.2022.100112.
- [30] T. Mai, M. Mowers, K. Eurek, Competitiveness Metrics for Electricity System Technologies, Technical Report NREL/TP-6A20-72549, National Renewable Energy Laboratory, Golden, CO, USA, 2021. URL: <https://www.nrel.gov/docs/fy21osti/72549.pdf>.
- [31] D. Meng, S. Yang, A. M. P. de Jesus, S.-P. Zhu, A novel Kriging-model-assisted reliability-based multidisciplinary design optimization strategy and its application in the offshore wind turbine tower, *Renewable Energy* 203 (2023) 407–420. doi:10.1016/j.renene.2022.12.062.
- [32] T. Cui, J. T. Allison, P. Wang, A comparative study of formulations and algorithms for reliability-based co-design problems, *Journal of Mechanical Design* 142 (2020) 031104. doi:10.1115/1.4045299.
- [33] X. Du, L. Burlion, O. Bilgen, Control co-design for rotor blades of floating offshore wind turbines, in: *ASME International Mechanical Engineering Congress and Exposition. Volume 7A: Dynamics, Vibration, and Control*, IMECE2020-24605, Virtual, Online, 2020, p. V07AT07A052. doi:10.1115/IMECE2020-24605.
- [34] F. Lemmer, K. Müller, W. Yu, D. Schlipf, P. W. Cheng, Optimization of floating offshore wind turbine platforms with a self-tuning controller, in: *ASME International Conference on Offshore Mechanics and Arctic Engineering*, OMAE2017-62038, Trondheim, Norway, 2017, p. V010T09A080. doi:10.1115/OMAE2017-62038.
- [35] J. López Muro, X. Du, J.-P. Condomines, et al., Wind turbine tower thickness and blade pitch control co-design optimization, in: *AIAA SCITECH 2022 Forum*, AIAA 2022-1150, San Diego, CA, USA and Virtual, 2022, p. 1150. doi:10.2514/6.2022-1150.
- [36] T. Cui, J. T. Allison, P. Wang, Reliability-based control co-design of horizontal axis wind turbines, *Structural and Multidisciplinary Optimization* 64 (2021) 3653–3679. doi:10.1007/s00158-021-03046-3.

- [37] A. P. J. Stanley, C. J. Bay, P. Fleming, Enabling control co-design of the next generation of wind power plants, *Wind Energy Science* 8 (2023) 1341–1350. doi:10.5194/wes-8-1341-2023.
- [38] F. Lemmer, W. Yu, B. Luhmann, et al., Multibody modeling for concept-level floating offshore wind turbine design, *Multibody System Dynamics* 49 (2020) 203–236. doi:10.1007/s11044-020-09729-x.
- [39] J. M. Jonkman, A. D. Wright, G. J. Hayman, A. N. Robertson, Full-system linearization for floating offshore wind turbines in OpenFAST, in: *ASME International Offshore Wind Technical Conference, IOWTC2018-1025*, San Francisco, CA, USA, 2018, p. V001T01A028. doi:10.1115/IOWTC2018-1025.
- [40] Y. H. Lee, S. Bayat, J. T. Allison, Control co-design using a nonlinear wind turbine dynamic model based on OpenFAST linearization, in: *MIT Applied Energy Symposium (MIT A+B)*, 6172, Cambridge, MA, USA, 2022.
- [41] M. M. Hand, M. J. Balas, Non-linear and linear model based controller design for variable-speed wind turbines, in: *Proceedings of FEDSM'99: 3rd ASME/JSME Joint Fluids Engineering Conference, FEDSM99-S295-11*, San Francisco, CA, USA, 1999, pp. 1–6. <https://www.nrel.gov/docs/fy99osti/26244.pdf>.
- [42] E. Branlard, J. M. Jonkman, S. Dana, P. Doubrawa, A digital twin based on OpenFAST linearizations for real-time load and fatigue estimation of land-based turbines, *Journal of Physics: Conference Series* 1618 (2020) 022030. doi:10.1088/1742-6596/1618/2/022030.
- [43] J. M. Jonkman, E. S. P. Branlard, J. P. Jasa, Influence of wind turbine design parameters on linearized physics-based models in OpenFAST, *Wind Energy Science* 7 (2022) 559–571. doi:10.5194/wes-7-559-2022.
- [44] O. E. Beshbichi, Y. Xing, M. C. Ong, Linear quadratic regulator optimal control of two-rotor wind turbine mounted on spar-type floating platform, *Journal of Offshore Mechanics and Arctic Engineering* 145 (2023) 022001. doi:10.1115/1.4055552.
- [45] J. Jonkman, A. Wright, G. Barter, M. Hall, J. Allison, D. R. Herber, Functional requirements for the WEIS toolset to enable controls co-design of floating offshore wind turbines, in: *ASME International Conference on Offshore Mechanics and Arctic Engineering, IOWTC2021-3533*, Virtual, Online, 2021, p. V001T01A007. doi:10.1115/IOWTC2021-3533.
- [46] J. M. Jonkman, The new modularization framework for the FAST wind turbine CAE tool, in: *51st AIAA Aerospace Sciences Meeting including the New Horizons Forum and Aerospace Exposition, AIAA 2013-0202*, Grapevine, TX, USA, 2013, pp. 1–26. doi:10.2514/6.2013-202.
- [47] B. C. Owens, J. E. Hurtado, J. A. Paquette, et al., Aeroelastic modeling of large off-shore vertical-axis wind turbines: Development of the offshore wind energy simulation toolkit, in: *54th AIAA/ASME/ASCE/AHS/ASC Structures, Structural Dynamics, and Materials Conference, AIAA 2013-1552*, Boston, MA, USA, 2013, pp. 1–14. doi:10.2514/6.2013-1552.
- [48] A. Beardsell, A. Alexandre, B. Child, et al., Beyond OC5 - further advances in floating wind turbine modelling using Bladed, *Journal of Physics: Conference Series* 1102 (2018) 012023. doi:10.1088/1742-6596/1102/1/012023.

- [49] J. T. Allison, A. Kaitharath, D. R. Herber, Wave energy extraction maximization using direct transcription, in: ASME International Mechanical Engineering Congress and Exposition. Volume 3: Design, Materials and Manufacturing, Parts A, B, and C, IMECE2012-86619, Houston, TX, USA, 2012, pp. 485–495. doi:10.1115/IMECE2012-86619.
- [50] L. T. Biegler, Nonlinear Programming: Concepts, Algorithms, and Applications to Chemical Processes, Society for Industrial and Applied Mathematics, Philadelphia, PA, 2010. doi:10.1137/1.9780898719383, isbn:978-0-89871-702-0.
- [51] J. T. Allison, D. R. Herber, Special section on multidisciplinary design optimization: Multidisciplinary design optimization of dynamic engineering systems, *AIAA Journal* 52 (2014) 691–710. doi:10.2514/1.J052182.
- [52] S. Bayat, J. T. Allison, LGR-MPC: A user-friendly software based on Legendre-Gauss-Radau pseudo spectral method for solving model predictive control problems, *arXiv preprint* (2023). arXiv:2310.15960.
- [53] S. Bayat, J. T. Allison, SS-MPC: A user-friendly software based on single shooting optimization to solve model predictive control problems, *Software Impacts* 17 (2023) 100566. doi:10.1016/j.simpa.2023.100566.
- [54] T. Lefebvre, F. De Belie, G. Crevecoeur, A trajectory-based sampling strategy for sequentially refined metamodel management of metamodel-based dynamic optimization in mechatronics, *Optimal Control Applications and Methods* 39 (2018) 1786–1801. doi:10.1002/oca.2442.
- [55] P. Qiao, Y. Wu, J. Ding, Q. Zhang, A new sequential sampling method of surrogate models for design and optimization of dynamic systems, *Mechanism and Machine Theory* 158 (2021) 104248. doi:10.1016/j.mechmachtheory.2021.104248.
- [56] Q. Zhang, Y. Wu, L. Lu, A novel surrogate model-based solving framework for the black-box dynamic co-design and optimization problem in the dynamic system, *Mathematics* 10 (2022). doi:10.3390/math10183239.
- [57] A. Sundarrajan, D. R. Herber, Using high-fidelity time-domain simulation data to construct multi-fidelity state derivative function surrogate models for use in control and optimization, in: ASME International Mechanical Engineering Congress and Exposition. Volume 6: Dynamics, Vibration, and Control, IMECE2023-112316, New Orleans, LA, 2023, p. V006T07A089. doi:10.1115/IMECE2023-112316.
- [58] E. Gaertner, J. Rinker, L. Sethuraman, et al., Definition of the IEA 15-Megawatt Offshore Reference Wind Turbine, Technical Report NREL/TP-5000-75698, National Renewable Energy Laboratory, Golden, CO, 2020. URL: <https://www.nrel.gov/docs/fy20osti/75698.pdf>.
- [59] A. B. Lambe, J. R. R. A. Martins, Extensions to the design structure matrix for the description of multidisciplinary design, analysis, and optimization processes, *Structural and Multidisciplinary Optimization* 46 (2012) 273–284. doi:10.1007/s00158-012-0763-y.
- [60] R. Jin, W. Chen, A. Sudjianto, An efficient algorithm for constructing optimal design of computer experiments, *Journal of Statistical Planning and Inference* 134 (2005) 268–287. doi:10.1016/j.jspi.2004.02.014.

- [61] G. Gualtieri, S. Secci, Methods to extrapolate wind resource to the turbine hub height based on power law: A 1-h wind speed vs. Weibull distribution extrapolation comparison, *Renewable Energy* 43 (2012) 183–200. doi:10.1016/j.renene.2011.12.022.
- [62] IEC, Wind energy generation systems – Part 3-1: Design requirements for fixed offshore wind turbines, Technical Report IEC 61400-3-1:2019, International Electrotechnical Commission, 2019. isbn:978-2-8322-7609-9.
- [63] K. Dykes, P. Graf, G. Scott, et al., Introducing WISDEM: An Integrated System Model of Wind Turbines and Plants, Technical Report NREL/PR-5000-63564, National Renewable Energy Laboratory, Golden, CO, 2015. URL: <https://www.nrel.gov/docs/fy15osti/63564.pdf>.
- [64] L. Fingersh, M. Hand, A. Laxson, Wind Turbine Design Cost and Scaling Model, Technical Report NREL/TP-500-40566, National Renewable Energy Laboratory, Golden, CO, 2006. URL: <https://digital.library.unt.edu/ark:/67531/metadc886232/>.
- [65] R. Harrison, G. Jenkins, Cost Modeling of Horizontal Axis Wind Turbines, Technical Report ETSU/W-34-00170-REP, University of Sunderland, School of Environment, Sunderland, UK, 1993. URL: <https://www.osti.gov/etdeweb/biblio/7202468>.
- [66] D. J. Malcolm, A. C. Hansen, WindPACT Turbine Rotor Design Study: June 2000 – June 2002, Technical Report NREL/SR-500-32495, National Renewable Energy Laboratory, Golden, CO, 2006. URL: <https://digital.library.unt.edu/ark:/67531/metadc1395424/>.
- [67] B. Maples, M. Hand, W. Musial, Comparative Assessment of Direct Drive High Temperature Superconducting Generators in Multi-Megawatt Class Wind Turbines, Technical Report NREL/TP-5000-49086, National Renewable Energy Laboratory, Golden, CO, 2010. URL: <https://digital.library.unt.edu/ark:/67531/metadc1012157/>.
- [68] NREL WISDEM Team, WISDEM Documentation, Manual, National Renewable Energy Laboratory, Golden, CO, 2019. URL: <https://wisdem.readthedocs.io>.